A NEW PERSPECTIVE ON DENSITY AND STRENGTH LOSS PROFILES AT THE SURFACE OF THERMALLY OXIDIZED NUCLEAR GRAPHITE

Cristian I. Contescu*[,1,2,#], James B. Spicer[2], Lianshan Lin[1], Jose D. Arregui-Mena[1], and Nidia C. Gallego*[,1]

[1]Oak Ridge National Laboratory, Oak Ridge, TN 37831, USA
[2]Johns Hopkins University, Baltimore, MD 21218, USA

[#]Retired

Abstract

Oxidation of graphite components could influence their designed life in a high-temperature nuclear reactor. The oxidized regions could potentially lower the allowed stress capacity. The American Society of Mechanical Engineers rules for the design and construction of graphite-moderated reactors recommend that subsurface regions that might become excessively damaged by oxidation during reactor operation be identified and excluded from geometry and stress calculations. Identification of oxidation-affected regions is possible, in principle, through complex modeling exercises of reactor behavior during hypothetical accident scenarios coupled with graphite oxidation models, but this procedure may not have the precision needed for informed decisions. This paper proposes an alternate method, based on interpretation of a series of well-designed oxidation experiments, which could augment the designer's tools. The procedure is illustrated by data on oxidation by air of several graphite grades (NBG-18, PCEA, IG-110, R4-650) that are corroborated with independent literature information, when available. The Wichner model for graphite oxidation used for this analysis provides conservative results that could be quickly implemented in the design process.

* Corresponding authors E-mail addresses:
ccontescu@comcast.net (Cristian. I. Contescu,
gallegonc@ornl.gov (Nidia C. Gallego)

1. INTRODUCTION

Modular high-temperature gas-cooled reactors (MHTGRs) are one of the inherently safe reactor designs selected for collaborative development and deployment through the Generation IV International Forum. In the United States, the US Department of Energy (DOE) supports and facilitates sharing graphite oxidation research results, the American Society of Mechanical Engineers (ASME) and ASTM International (ASTM) develop and adopt by consensus the codes and standards for graphite components' design and construction, and the US Nuclear Regulatory Commission (NRC) licenses and inspects commercial power reactors. However, the licensee has the ultimate responsibility for the reactor's performance and safe operation. Close interactions between the designer and the manufacturer of the graphite components during design, construction, and reactor operation are expected to ensure safe and cost-effective operations throughout the reactor's life [1].

The intrinsic safety of MHTGRs relies on multiple protection barriers, from the ceramic layers protecting tristructural-isotropic (TRISO) fuel, supplemented by more confining barriers of matrix carbon and in-core graphite components, to the helium pressure boundary and the reactor building. Safety is augmented by passive control of critical operations accomplished with minimal (or no) reliance on active systems or operator actions [2]. Graphite structures do not have pressure containing function, but they are essential for maintaining reactor structural integrity and functionality during decades of operation. The safety rules related to structural integrity are consensually agreed upon by the Boiler and Pressure Vessel Committee affiliated with ASME [3].

High-purity, high-density polycrystalline synthetic graphite is ideally suited as a neutron moderator in MHTGRs because of its remarkable ability to thermalize high-energy neutrons, combined with high thermal stability, low thermal expansion, high thermal conductivity, convenient machinability, and large-scale availability. However, graphite components may be subjected to chemical reactions and degradation by oxidants at reactor operational temperatures. Oxygen is the highest concern because of its high reactivity. Using the rate of carbon oxidation by CO_2 at 800 °C and 0.1 bar partial pressure as reference, oxidation by H_2O is only 3 times faster, whereas oxidation by O_2 is about 100,000 times faster [4]. This difference separates graphite oxidation events of interest to reactors' safety and graphite functionality into two

categories: (1) slow (chronic) oxidation during normal operation by H_2O or CO_2 traces in the helium coolant and (2) rapid (acute) oxidation after an unlikely air-ingress accident. Off-normal events are ranked based on their occurrence probability [5] and radiation effects at the site boundary [6]. In the order of decreasing probability, transient deviations from normal operation conditions are classified [2] as anticipated events (AE; $< 10^{-2}$ per plant-year), design-basis events (DBE; $10^{-4} – 10^{-2}$ per plant-year), and beyond-design-basis events (BDBE; $5 \times 10^{-7} – 10^{-4}$ per plant-year).

Chronic oxidation by trace impurities in the helium coolant is generally considered to be negligible. Purified helium coolant in MHTGRs may still contain traces of oxidant species (such as < 0.04 ppm O_2, < 0.2 ppm H_2O, and < 0.6 ppm CO_2), reducing species (such as < 3 ppm H_2 and < 3 ppm CO), and inert species (< 0.2 ppm N_2, < 0.5 ppm CH_4) at 4 MPa total pressure and 800 – 950 °C outlet temperature [7]. Experiments [8] and simulations [9,10,11,12] indicate that, under normal operation conditions, these extremely low concentrations of impurities might very slowly oxidize only a thin layer (< 1 mm) at the surface of a few graphite fuel blocks at the bottom of the reactor during the reactor's lifetime.

More significant is the acute or severe oxidation caused by an unlikely air ingress accident. Postulated scenarios of various severity were devised to simulate hypothetical transients belonging to either DBE or BDBE accident situations. Although these scenarios have low or very low probability, because of the high risk involved, they have raised concerns about graphite behavior and prompted numerous analyses of hypothetical off-normal events. Investigators used computer codes [13,14] supported by laboratory measurements [15,16,17,18], modeling projects [19,20], thermohydraulic simulations of reactor gas environment [21,22,23,24], and large-scale experimental replicates of postulated accident situations [25,26] to assess the effects of these events. The results showed that massive air ingress accidents may cause oxidation of graphite components at the reactor base (bottom reflector and lower fuel elements) and even in the fueled region. Some regions of the affected graphite components may suffer strength loss damage exceeding the nominal fracture strength. Nevertheless, even in such extreme situations, sacrificial graphite oxidation at the reactor's bottom would reduce the oxygen supply to the middle and upper sections, thus preventing oxidation of matrix carbon that protects the TRISO fuel [27]. All analytical evaluations of BDBE massive ingress accidents confirmed

that the TRISO fuel likely will not be affected [28,29,30]. The sensitivity analyses of variables involved in postulated scenarios demonstrated that very low probability events are surrounded by high levels of uncertainty.

Chronic and acute oxidation discussed above are two extreme situations in the reactor's lifetime. However, limited graphite oxidation may also occur between these extremes, during either AE or DBE conditions. Two examples were discussed in a recent Idaho National Laboratory report [27]. In a DBE scenario, a small breach in the pressurized helium boundary would be followed by air ingress for 40 days. Corresponding to the limited amount of fresh air ingress (267 kg), only 0.008 % of the total graphite in the reactor would be oxidized. In another DBE example, a small leak in the steam generator system would allow a moderate ingress of 272 kg steam for several hours; only about 75 kg of this steam would oxidize 50 kg of graphite. As in the case of air ingress, the global graphite oxidation would affect just 0.04 % of the total structural graphite mass, resulting in an insignificant local 0.5% loss of strength in the coolant graphite channels. Those events were not regarded as immediate safety issues because of the limited amount of graphite oxidation [2].

In principle, oxidation of individual graphite components in MHTGRs and their effect on safe operation could be estimated for designer-selected boundary conditions (incident type and frequency, leakage rates, heat-removal procedures, timeline of remediation actions) and graphite-specific oxidation models based on experimental measurements. This process requires correlating detailed graphite oxidation models with anticipated information on flow and temperature distributions based on knowledge of the reactor's overall behavior. Such data depend on numerous unknowns. Some relate to the distribution and evolution of flow rates, temperatures, pressures, and local gas compositions at various sections of the reactor. Others are problematic because of continuously changing graphite properties (porosity, active surface area, density profile) with the progress of oxidation. Most of the global analyses referenced above have been done this way. However, a more focused approach—estimating not only **where** and **how much** graphite oxidation may have occurred but also the **extent of properties damage—** might be necessary.

The remainder of this paper focuses on the graphite oxidation effects on exposed regions of graphite components, in particular the local decrement of density and mechanical strength.

First, the traditional ways of systemic modeling of graphite oxidation in the context of various accident scenarios will be briefly reviewed. Multiple sources of epistemic and aleatory uncertainties of such global analysis, which may affect the conclusions' reliability, call for better understanding of interacting factors and mechanisms. Second, this paper describes an experiment-based procedure for evaluating oxidation consequences on graphite properties, supported by a fresh analysis of the authors' prior oxidation results corroborated with other literature information. The graphite components designer may benefit from this practical approach, which involves a well-conceived and executed experimental program.

2. ASME CODE REQUIREMENTS

Oxidation will remove material from the surface of graphite components, thereby reducing the fracture toughness, strength, and elastic properties of the graphite and modifying its thermal conductivity. Oxidation might also cause dimensional shrinking and loss of physical integrity, seriously affecting safe operation and functionality of graphite components. The safety rules for maintaining the integrity and functionality of individual graphite core components and graphite core assembly, with special attention to properties degradation caused by neutron irradiation and oxidation can be found in the ASME Boiler and Pressure Vessel Code (BPVC), Section III, Division 5 [3].

Given that oxidation rates depend on temperature, reactants, and graphite grade, the rules related to oxidation require detailed estimation of weight loss profiles of those graphite structures that might be affected. Considering strength reduction, the rules require identifying and excluding from stress calculation those oxidized regions where strength decreases below some critical limits from the unoxidized graphite strength. Regarding geometry changes upon oxidation, the rules also require the designer to determine the weight loss threshold above which the oxidized regions should be considered as completely removed from the surface. The code also recommends using the relationship between weight loss (or density loss) and strength decay, as illustrated by a nonmandatory diagram provided as an example for which 10% local weight loss correlates with about 50 % compressive strength loss. Because this quite aggressive compressive strength decay might not generally hold for some graphite grades, the code requires that the relationship between the properties of interest (compressive and tensile strength, Young's

modulus, thermal conductivity) and the weight loss of *uniformly* oxidized specimens must be experimentally determined for each new graphite grade.

At this point it is useful to clarify the two meanings of "weight loss" in the context of graphite oxidation analysis. Generally, weight loss refers to the global mass change recorded during oxidation, WL = $\Delta m/m_0 \times 100$ %. According to this global definition, WL is a conditional value that depends on the size (and initial mass, m_0) of graphite specimens. Oxidation propagates from the exposed surfaces, and ratios of surface area to volume are smaller for larger components; therefore, at equal oxidation conditions and similar geometries, larger components would have smaller WL values than laboratory-scale small specimens used in experiments. In large components, such as graphite core-support columns (Ø21 cm in CT-MHR [31], Ø15 cm in HTTR [32]), oxidation will produce a measurable weight loss profile that (in absence of dimensional changes by surface corrosion) is equivalent to a density profile. In similar oxidation conditions, such a profile may look completely different for small laboratory specimens if the oxidation penetration depth is comparable to the specimens' dimensions. To avoid confusion, the WL notation will be used for the *global mass changes* (either measured or predicted for laboratory graphite specimens of full-size graphite components), distinct from *local profiles* of oxidant concentration, weight loss, density, or other physical properties in the subsurface oxidized zone.

3. THE TRADITIONAL WAY OF GLOBAL ANALYSIS

Predicting **where** and **how much** oxidation may have occurred after an unlikely DBE or BDBE air ingress is a daunting task. First, simulations must be designed to model fluid flow, composition, and temperature transfer at the reactor scale. These simulations should reliably calculate evolution of oxidation processes over time scales of many days (not hours, as is common for liquid water reactors). Considering that depressurization triggers helium outflow followed by (or simultaneously with) air inflow, the models should include reactor-scale analysis of natural circulation of gases, passive heat decay, and heat evolution from exothermic oxidation reactions. For pebble-bed reactor designs, heat transfer and gas flow in packed-bed configurations must also be modeled. In the United States, systemic reactor analysis has been performed using traditional computer codes supplemented with fluid dynamics codes (e.g.,

FLUENT). In parallel, national laboratories have built custom codes, such as ORECA and MORECA (used for safety analysis of Fort St.-Vrain HTGR reactor), which were later developed into the GRSAC code [33]. The latter was validated by successful modeling of past accidents (Chernobyl, Windscale) and was further used to model postulated events in various reactor designs [14]. Other specialized codes, such as MELCOR [34], GAMMA [35], and RELAP5 [36] were developed for modeling various aspects of HTGR-specific accident scenarios.

When possible, simulations combine transient thermal-hydraulic conditions at specific nodes of a reactor's structure with estimates of graphite oxidation progression as a function of local conditions (temperature, oxidant supply rate, gas flow character) and time. The main factors affecting major core damage are the size and position of hypothetic system leaks, gas flow characteristics, gas chemistry, and temperature distribution, but these factors are difficult to estimate accurately [37]. Next, thermal-hydraulic simulations must be interfaced with graphite oxidation models to evaluate the rate and extent of oxidation of critically exposed graphite components. A recent review of various strategies used for graphite oxidation modeling is available elsewhere [38]. Once spatial representations of density profiles and dimensional changes have been obtained for graphite components of specific shape and size, at preselected locations in the reactor, and for postulated ingress scenarios of various severity, then the calculated profiles of density or local weight loss in the oxidized graphite should be converted into strength profiles. That would eventually identify oxidized graphite regions that must be excluded from stress calculations or regarded as completely detached. This complex procedure is inherently plagued by epistemic and aleatory uncertainties related to the initial transient event assumptions, computational simplifications of oxidation models, and the imperfect knowledge of graphite properties' evolution during oxidation. Currently, very little is known about the effects of neutron irradiation on graphite oxidation behavior. A condensed presentation of graphite oxidation mechanisms and the parameters required for quantitative modeling is available in Appendix A.

4. A SIMPLER AND PRACTICAL ALTERNATIVE

During the last few decades, graphite oxidation models have improved significantly. Expanded availability of more experimental data made it possible to derive well-parametrized

kinetic and diffusion rate equations for specific graphite grades. However, consistent experimental verification of advanced oxidation models against repeated runs in various conditions with graphite bodies of various shapes and sizes remains an unmet necessity. Generally, demonstrating a model's ability to reproduce preexisting experimental data is easier than using the same model for ab initio predictions of future experimental results. When the limitations of existing oxidation models are correlated with the recognized ambiguity associated with real-time description of postulated events by full-scale computer codes, the detailed oxidation analysis mandated by the ASME code appears as an intimidating task.

An alternative analysis adapted from Wichner's model for graphite oxidation [39] may supplement the designer's toolbox with an experiment-grounded evaluation of critical properties changes in oxidized graphite. Rather than relying on complex exercises from global air-ingress scenarios interfaced with local oxidation models, a new perspective on the temperature effects on density profiles and properties decay in oxidized graphite can be obtained by building a database of graphite samples oxidized in well controlled conditions. In this approach, general trends of oxidation behavior of each graphite grade of interest shall be obtained by analyzing the results of three sets of well-designed and carefully executed experiments. First, the *kinetic parameters* of chemically controlled oxidation reactions should be determined from oxidation rate measurements according to ASTM D7542 [40]. Second, several *sufficiently large specimens* (to allow full development of oxidized profiles) should be oxidized at various temperatures, and their *density profiles* in subsurface oxidized zones should be characterized. Third, *small size specimens oxidized uniformly* in conditions in which volume oxidation prevails (slow oxidation at low temperatures) should be used to determine the decay rate of the *properties of interest* (strength, modulus, thermal conductivity) vs. the average WL. All these data may be used to convert local weight loss (or density) profiles of oxidized specimens into local subsurface strength decay profiles, and to estimate their evolution as a function of oxidation temperature. According to the ASME code [3], highly oxidized regions should be regarded as totally detached and should not be credited for stress calculations. The results of this analysis will provide the designer useful information for identification of potentially excluded oxidized surface regions, correlated with the respective oxidation rates at any oxidative conditions within the qualification envelope range. A few simplifying assumptions of the proposed analysis will ensure that the conclusions are conservative.

Wichner's model for graphite oxidation [19,39] is based on simultaneous analysis of diffusion and chemical reactions in porous materials [15]. In summary, the oxidant transport in graphite's pores is assumed to follow Fick's laws of diffusion and establish a concentration profile decreasing exponentially from the exposed surface into the bulk. In competition with diffusion, oxidant consumption by chemical reactions tends to shrink the concentration profile, limiting its advancement farther from the surface. Supported by a few simplifying, but conservative, assumptions (Appendix A), a time-independent quasi-steady state is obtained from these opposing trends. At constant temperature, a nearly stable oxidant concentration profile in the active oxidation zone is described by a decaying exponential that depends on the ratio between oxidant reactivity and diffusivity:

$$\frac{C(x)}{C_0} = \exp\left(-x\sqrt{\frac{A(T)}{D_{\text{eff}}(T)}}\right). \quad (1)$$

Here, C(x) is the oxidant concentration at distance x from the surface, C_0 is the oxidant concentration at the surface (at x = 0). Under the square root sign, $A(T)$ is the reactivity factor which collects temperature-dependent factors in the chemical rate equation, the frequency factor, and some graphite physical properties introduced for unit normalization:

$$A(T) = k_0 \mathrm{R}T\exp\left(-\frac{E_a}{\mathrm{R}T}\right)\frac{\rho}{\varepsilon}F_b N(T), \quad (2)$$

where, E_a (J/mol) is the apparent activation energy, and k_0 (Pa^{-1} s^{-1}) is a frequency factor. They are calculated, respectively, from the slope and the intercept of the Arrhenius plots describing the effect of temperature on experimental oxidation rates. Graphite properties are represented by the molar density ρ (mol m^{-3}), the porosity fraction ε (m^3-void/m^3-graphite), a factor (F_b) describing reaction rate acceleration on the increase of WL, and the stoichiometric ratio of CO/CO_2 products of carbon reactions, $N(T)$, which depends on temperature; T (K) is the oxidation temperature, and R is the gas constant.

Information on graphite reactivity is available from oxidation rate measurements as a function of temperature, but the reactivity factor $A(T)$ should not be confused with the global oxidation rate, $OR(T) = Zexp(-E_a/RT)$, measured between 5 and 10 % WL according to ASTM D7542 [40]. As explained in Appendix A, the experimental oxidation rates at any temperature T are the

product of temperature-dependent factors contained in $A(T)$ and the partial pressure of O_2 in free gas near the graphite surface, P_{O2}. The latter is a circumstantial parameter which may significantly vary during air-ingress transient events. Inside the active oxidation zone in graphite, the distribution of oxygen concentration is nonuniform, as determined by the competition between the rates of O_2 supply (diffusion) and consumption (reactions). When diffusion and carbon reaction rates come to parity, a quasi-stable O_2 concentration profile is achieved, and a nearly constant global oxidation rate is observed, usually between 5 and 10 % WL. At that condition, the local O_2 concentration determined by diffusion is used for calculation of the density profile in the oxidized zone.

The other term under the square root in eq. (1), $D_{eff}(T)$, is the oxidant effective diffusivity through the graphite pore network. Both reactivity and effective diffusivity are temperature dependent, but in different ways: $A \propto \exp(-1/T)$ and $D_{\text{eff}} \propto T^q$. Information on chemical reactivity is available from oxidation rate measurements adhering to ASTM D7542 [40], but information on effective diffusivity is missing. Gas diffusion in graphite's tortuous pore structure should reflect free gas diffusion, proportionally reduced by a factor specific to the pore system properties. An effective diffusivity given by Eq. (3) is assumed for each graphite grade:

$$D_{\text{eff}}(T) = \beta D_0(T), \tag{3}$$

where the structure factor $\beta \ll 1$ depends on graphite microstructure, and D_0 is the free gas diffusion coefficient of oxygen in air: $D_0 = 1.78 \times 10^5$ m^2/s at 273 K and 760 Torr (101.325 kPa) [41]. For oxygen, D_0 increases proportionally with $T^{1.75}$ and varies inversely with total gas pressure:

$$D_o(T,P) = 1.78 \times 10^5 \left(\frac{T}{273}\right)^{1.75} \left(\frac{101.325}{P}\right), \tag{4}$$

where T (K) and P (kPa) are the temperature and total gas pressure at oxidation conditions. The following calculations assume that the oxygen partial pressure during oxidation rates measurements at ORNL was $P_{O2} = 21.3$ kPa (i.e., 21 % of atmospheric pressure at sea level). The effective diffusivity D_{eff} of each graphite grade has the same temperature behavior as D_0, but the grade-dependent structure factors β are not known. Moreover, β is expected to vary with the progression of oxidation as the newly developed porosity reduces diffusion resistance.

The value of D_{eff}, and thus β, can be obtained from experimental correlations derived from Eq. (1), provided that all information contained in *A(T)* is available from rate measurements and initial graphite characterization. The structure factor β is estimated by analyzing the temperature effect on maximum oxidant penetration depth or on the local graphite density profiles in oxidized layers at steady state. With a few conservative simplifying assumptions (discussed below), analytical solutions can be derived for generalization of conclusions.

Historically, the semi-empirical approach of using an effective diffusion coefficient was demonstrated as a practical solution for graphite oxidation problems [42, 43, 44]. However, the prospect of a parallel Knudsen diffusion mechanism coexisting with molecular diffusion at oxidation conditions has been recently reanalyzed by Kane et al. based on a new series of experimental measurements [45]. Indeed, for conditions associated with oxidation, the mean free path of O_2 molecules (0.97 – 1.32 μm from 550 to 850 °C) is much larger than the mesopores size range in nuclear graphites (0.005 – 0.05 μm), allowing gas molecules to collide with the mesopore walls (Knudsen mechanism). However, mesopores represent just a small fraction of the total volume of open pores in nuclear graphites (Table 1). After oxidation, mesopore volumes increase (e.g., up to 20 times for IG-110 from our data), but the volumes of large and very large macropores increased substantially more. Moreover, the diffusion coefficient for molecular diffusion increases faster with temperature ($D_0 \propto T^{1.5}$) than Knudsen diffusion coefficient ($D_K \propto T^{0.5}$). Both these arguments support Wichner's original conclusion that Knudsen diffusion can safely be disregarded in graphite oxidation models. [39]

5. STEADY STATE

Equation (1) describes the oxidant concentration profile in the active oxidation zone corresponding to the nearly stable concentration distribution established after a long time. Mathematically, Eq. (1) is the solution at $t \rightarrow \infty$ of the differential equation describing the mass balance in a process with simultaneous reactant diffusion and chemical reaction (Appendix A). The notion of a quasi-steady state oxidation process is obviously an approximation. The dynamic equilibrium between oxidant transport and consumption is assumed to create a stationary oxidant concentration profile. This profile defines the active oxidation zone, where carbon material is

continuously removed at temperature-dependent rates proportional to the local oxidant concentration. For slow oxidation at low temperatures (Regime 1), a reasonable assumption is that the oxidant concentration profile evolves toward its fully developed shape, which may extend deep into the bulk. Simultaneously, a reverse graphite density profile develops in the active oxidation zone (Fig. 1). At large values of x, the boundary conditions are

$$\lim_{x\to\infty} C(x) = 0\,, \tag{5}$$

and

$$\lim_{x\to\infty} \rho(x) = \rho_\infty\,, \tag{6}$$

where ρ_∞ is the unoxidized bulk density. With the increase in temperature (Regime 2), reactivity increases faster than diffusivity, thereby narrowing the oxidant concentration profile. As isothermal oxidation continues, the oxidant concentration profile moves slowly inward but retains its fully developed shape. At extremely high temperatures (Regime 3), fast surface oxidation is accompanied by surface corrosion and graphite volume shrinkage. After high-temperature oxidation (Regime 3), a low-density remnant surface zone left behind surface corrosion and dimensional shrinking was documented on badly corroded graphites. An example is shown in Fig. C.1 in Appendix C [46]. Alternatively, the corroded remnant may detach as a powder of spalled graphite grains after preferential oxidation of the graphite binder phase (Fig. 2) [17,47].

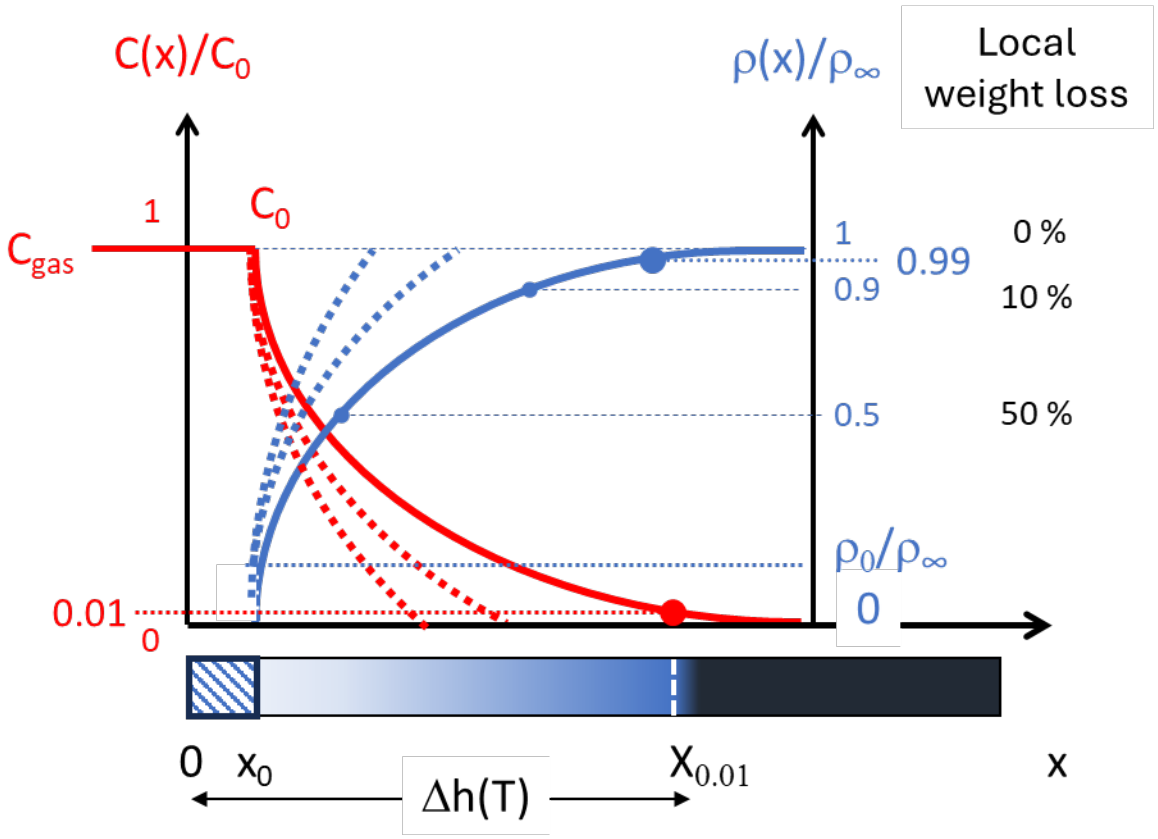

Fig. 1 Schematic representation of the oxidant concentration profile and the reverse density change profile in the active oxidation zone.

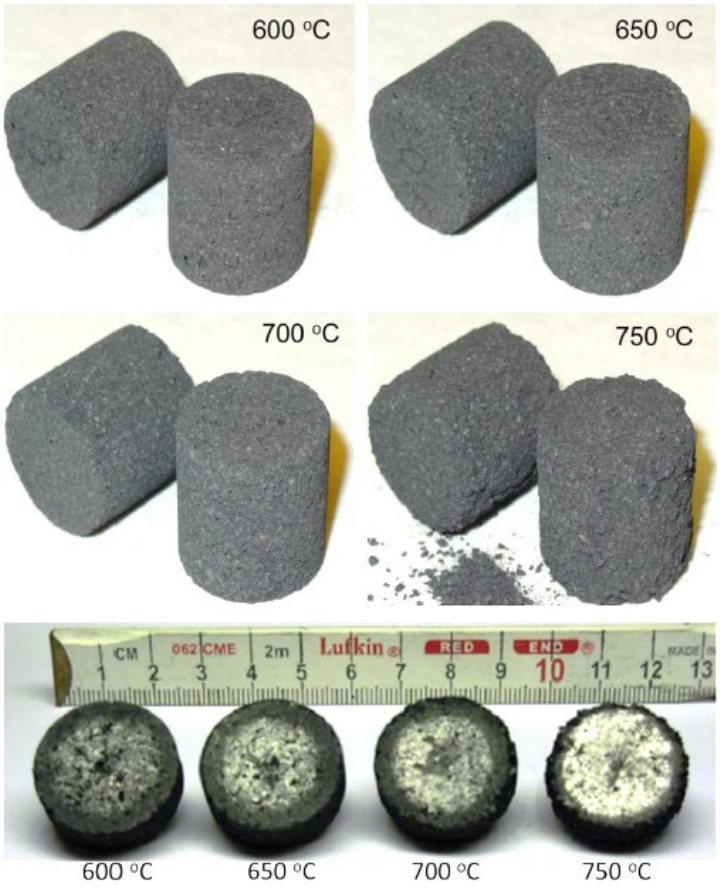

Fig. 2: Images of graphite NBG-18 specimens oxidized to 15% WL in air at four different temperatures. The cross-section photos of the same specimens in the bottom panel show variations of oxidized layer penetration depth. (Data adapted from refs. [17,47].)

The desired information is the graphite density profile at various oxidation conditions. Recall Eq. (1), which shows that the oxidant concentration decays exponentially with the distance from the surface; the rate of decay is $\left(A/D_{eff}\right)^{1/2}$. At steady state, the graphite density profile should conform to the oxidant concentration profile but in reverse. Therefore, the density profile is given by Eq. (7):

$$\rho(x) = \rho_\infty - (\rho_\infty - \rho_0)\left[\frac{C(x)}{C_0}\right], \tag{7}$$

where ρ_0 is the density of "fully" oxidized remnant, probably about 10 – 20 % of ρ_∞ (Fig. 1). At low and moderate temperatures (Regimes 1 and 2), oxidant concentration at $x = 0$ can be equated with its partial pressure in the free gas, $C_0 = C_{gas} = P_{gas}/RT$. At high temperatures (Regime 3), fast chemical rates place a great burden on mass transfer rates, so that C_0 is reduced from the free gas concentration by a factor depending on the rate of mass transfer through the boundary layer. More details are available elsewhere [19,39]. For the purpose of this simplified model, mass transfer limitations in the boundary layer characteristic to oxidation in Regime 3 are neglected.

Rearranging Eq. (1) yields a correlation between the oxidant concentration decay fraction, distance from surface, and temperature:

$$x = -\ln\left(\frac{C(x)}{C_0}\right)\sqrt{\frac{\beta D_0(T)}{A(T)}}. \qquad (8)$$

The "end" of the fully developed active oxidation zone can reasonably be assumed to occur at a distance X_δ from the surface where the local oxidant concentration is a small fraction, for example 0.01, of surface concentration (i.e., $\delta = C(X_\delta)/C_0 = 0.01$). If several direct measurements of maximum penetration depth X_δ at various temperatures are available, then the structural coefficient β can be obtained by regression from Eq. (8) and then used to estimate oxidized layer penetration depth at any other temperature, $X_\delta(T)$. Similarly, the temperature effect can be estimated for other δ values. For example, setting $\delta = 0.1$ allows mapping the temperature variation at distances x where the local density is reduced by 10 % (i.e., $\rho(x)/\rho_\infty = 0.9$). Such density profiles can be estimated at all temperatures from the operational parameters' envelope.

At the time when Wichner's simplified model was proposed, experimental data needed for such predictions were very limited. The remainder of this paper uses recent experimental information to demonstrate a method that could satisfy designer's needs regarding identification and exclusion from stress and geometry consideration of those surface regions where the decays of local density and strength after various postulated oxidation events would exceed certain design-related limits. In other words, any "corrosion (i.e., oxidation) allowance" of possible surface-damaged graphite components after an air ingress accident could be estimated based on a series of well-planned experiments.

6. EXAMPLES

6.1 Materials

Oxidation behavior of various graphite grades can be correlated with the nature of raw materials (petroleum or pitch coke) and specific microstructure differences related to the primary crystallites (graphitization, size, and orientation), filler grains (average shape and size), binder (degree of graphitization, structural homogeneity), and porosity (overall void fraction, size distribution, connectivity, and accessibility of open pores) [48,49,50]. For these many reasons, nuclear graphites exhibit grade-specific oxidation behavior which must be individually characterized. However, some general trends can be identified and parametrized to rationalize the temperature dependence of oxidation-induced damage in graphite.

The procedure presented below is based on a fresh analysis of experimental results from oxidation studies (some only partially published) at Oak Ridge National Laboratory (2005–2012). Three nuclear graphite grades (NBG-18, PCEA, and IG-110) and one used for continuous metal casting (R4-650) were investigated (Table 1).

Table 1: Main properties and experimentally derived results for selected graphite grades.

	IG-110	PCEA	R4-650	NBG-18
Bulk (apparent) graphite density (g/cm^3) [(a)]	1.76	1.77	1.835	1.86
Molar graphite density, ρ (kmol/m^3)	146.7	147.5	152.9	155.0
Skeleton density (g/cm^3) [(b)]	2.05	2.00	2.03	2.02
Total pore volume (cm^3/g) [(c)]	0.122	0.119	0.135	0.091
Open pore volume (cm^3/g) [(d)]	0.079	0.065	0.050	0.044
Mesopore volume (cm^3/g) [(e)]	0.001	0.002	n/a	0.002
Void fraction, ε [(f)]	0.214	0.210	0.248	0.170
Preexponential factor in Arrhenius plots, ln $Z_w(s^{-1})$ [(g)]	12.88	12.07	14.25	11.32
Frequency factor in Arrhenius equation, k_0 (Pa^{-1} s^{-1}) [(h)]	18.47	8.20	73.11	3.88
Activation energy in Arrhenius equation, E_a (kJ/mol) [(g)]	190.4	184.7	202.0	187.0
Structural factor of effective diffusivity, β [(i)]	0.020	0.004	0.006	0.005

(a) ρ_{bulk}, from direct weight and volume measurements.
(b) ρ_{sk} , from helium pycnometry.
(c) $V_t = \left(1/\rho_{bulk} - 1/\rho_{cryst}\right)$ where ρ_{cryst} = 2.24 g/cm^3 is the ideal graphite crystal density.
(d) $V_o = (1/\rho_{bulk} - 1/\rho_{sk})$
(e) Calculated from N_2 adsorption isotherms at 77 K.
(f) $\varepsilon = V_t \times \rho_{bulk}$.
(g) From plots of weight-normalized oxidation rates: $\ln[OR_w(s^{-1})] = \ln[Z_w(s^{-1})] - E_a/(\mathrm{R}T)$, see ASTM D7542.
(h) $k_0(\mathrm{Pa}^{-1}s^{-1}) = Z_w(s^{-1})/\ P_{O2}(\mathrm{Pa})$, where P_{O2} is oxygen partial pressure in free gas phase during oxidation.
(i) See Section 7.

6.2 Data collection and analysis

Oxidation in air of cylindrical specimens (Ø = h = 25.4 mm) was conducted in a vertical tube furnace according to ASTM D7542 [40]. The specimens were suspended from the below-balance weighing port of an analytical scale placed on a thermally insulated platform on top of the furnace. A fast supply (10 L/min) of dry air flow was maintained during isothermal oxidation to the desired weight loss, while the weight variation was continuously recorded. Fig. 3 shows weight variations vs. time at 600, 650, 700, and 750 °C. Characteristically, oxidation rates increase with the weight loss and later stabilize to near-constant values between 5 % and 10 % WL. The stable rates from duplicate runs at each temperature were plotted in Arrhenius coordinates (ln (*Rate*) vs. 1/*T*), and the apparent activation energies and preexponential factors were calculated for each graphite grade from the slope and intercept (Table 1). Note that the two ways for normalization of oxidation rates indicated by ASTM D7542 (by weight or by area) will

give the same activation energy but different results for the preexponential factor [40]. Data show that the oxidation reactivity increased in the order NBG-18 < R4-650 < PCEA < IG-110.

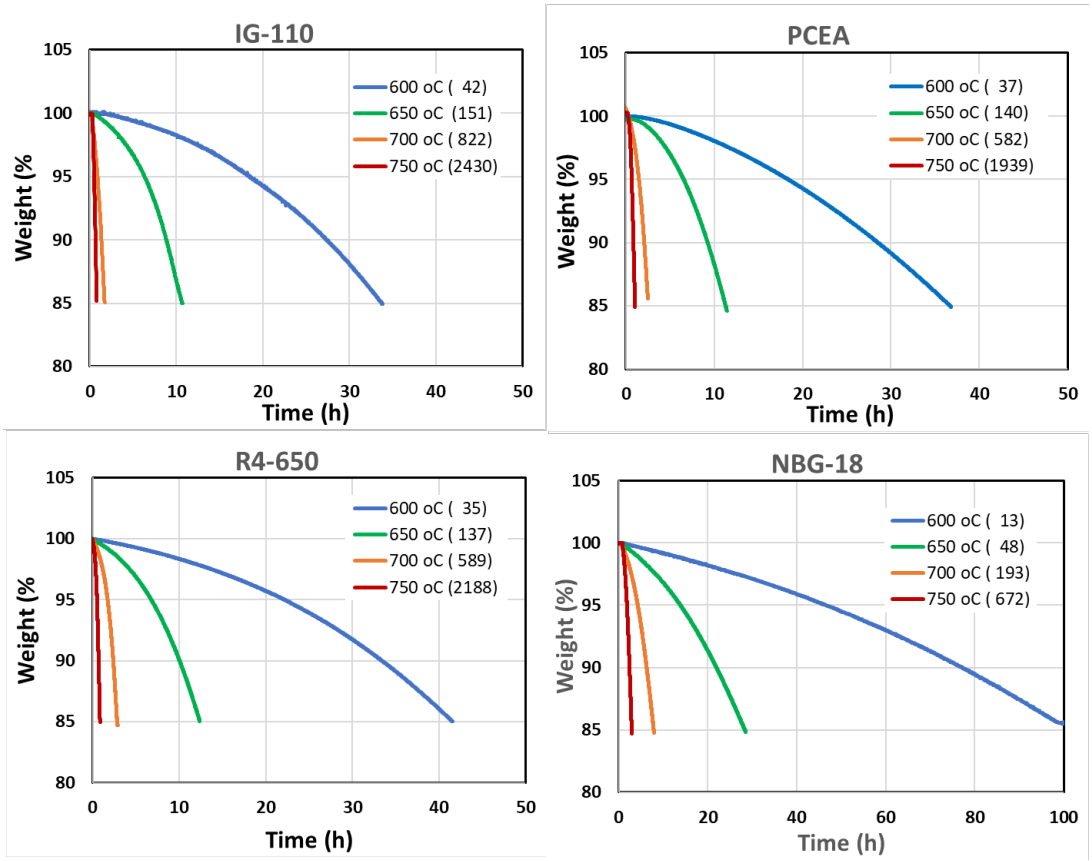

Fig. 3: Raw oxidation data showing reactivity differences between the four graphite grades. Legends show oxidation temperatures (°C) and (in brackets) the corresponding oxidation rates (g h^{-1} m^{-2}) calculated between 5 and 10 % WL. (Author's data, unpublished.)

Optical microscopy analysis of the oxidized layer was performed only for the three nuclear graphite grades (IG-110, PCEA and NBG-18). The specimens were cross-sectioned and examined at 400× magnification. Automated image analysis (Image Pro Plus software) was used to classify pores based on size and position relative to the exposed surface [17,47]. Figure 4 shows the steps used for visual identification and measurement of the oxidation penetration depth. The visual results were compared against pixel intensity profiles of the same regions. The

estimated errors of oxidation penetration length measurements vary between ± 0.5 mm to ± 0.1 mm, depending on the oxidation temperature and graphite microstructure.

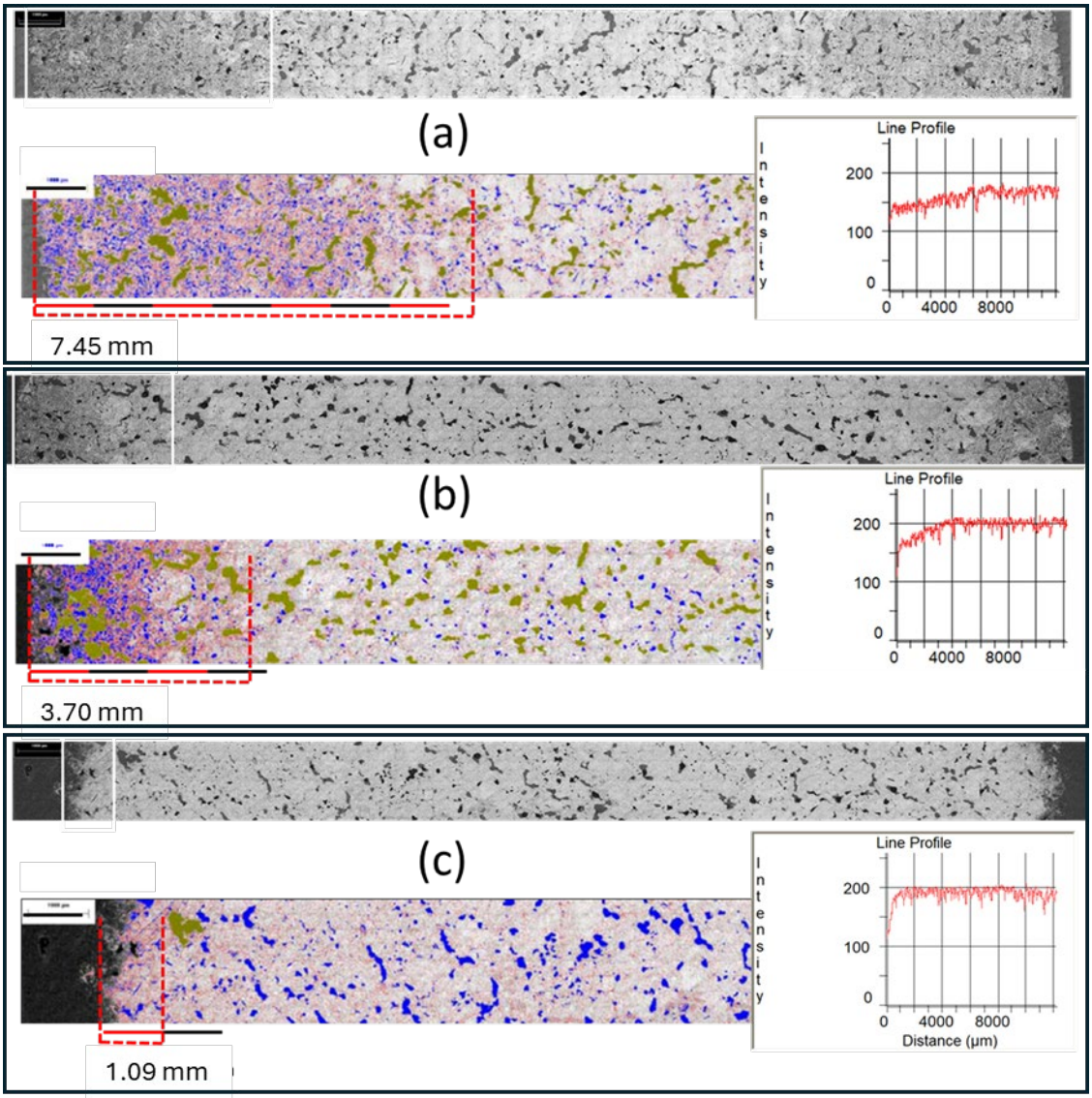

Fig. 4: Example of oxidized layer analysis showing results for PCEA specimens (Ø = h = 25.4 mm) oxidized to 15 % WL at (a) 600 °C; (b) 650 °C; and (c) 750 °C. A subsurface region was selected from one end of each black/white image, and the pores were identified, and code-colored based on their size. The oxidized zone was visually identified (as marked) and its length was measured. The selection was cross validated by the pixel intensity profile recorded over the half diameter (12 mm) of the corresponding black/white image. (Author's data, adapted from ref. [47].)

Figure 5 compares cross-sectional mosaic images of radial slices (12.5 × 1 mm^2) of nuclear graphite specimens oxidized at equal WL (15 %) and different temperatures (600 –750 °C); and at constant temperature (600 °C) and various WL levels (only for PCEA). The boundary between the non-oxidized and oxidized zone was more difficult to identify in graphite IG-110 (a fine-grain graphite with extremely small pores) compared with NBG-18 and PCEA medium-grain graphites.

Figure 6 shows pixel intensity distributions as a function of distance from the exposed surface in the oxidized layers of the three nuclear graphites. [17,47]. In this analysis, low pixel intensities in black-and-white images from low reflectivity areas are associated with open surface pores, while higher intensities represent high reflectivity, pore-free surfaces. Fig. B1 in Appendix B illustrates the evolution of pixel intensity profiles for PCEA specimens oxidized at three temperatures and four WL levels. In all images, the pixel size was 3.156 μm, which corresponds to 9.96 μm^2 for the minimum identifiable pore areas.

In addition to optical microscopy, density profiles of oxidized layers in graphite IG-110 [31,51], NBG-18 [18,52] and R4-650 [16] measured by the lathing method were also used in the study. Original data are shown in Appendix C. In this method, thin layers were removed in small steps from all sample surfaces, and the local density of each layer removed was calculated from careful weight and volume measurements. Quantitative density profile data from these measurements are discussed in Section 7.

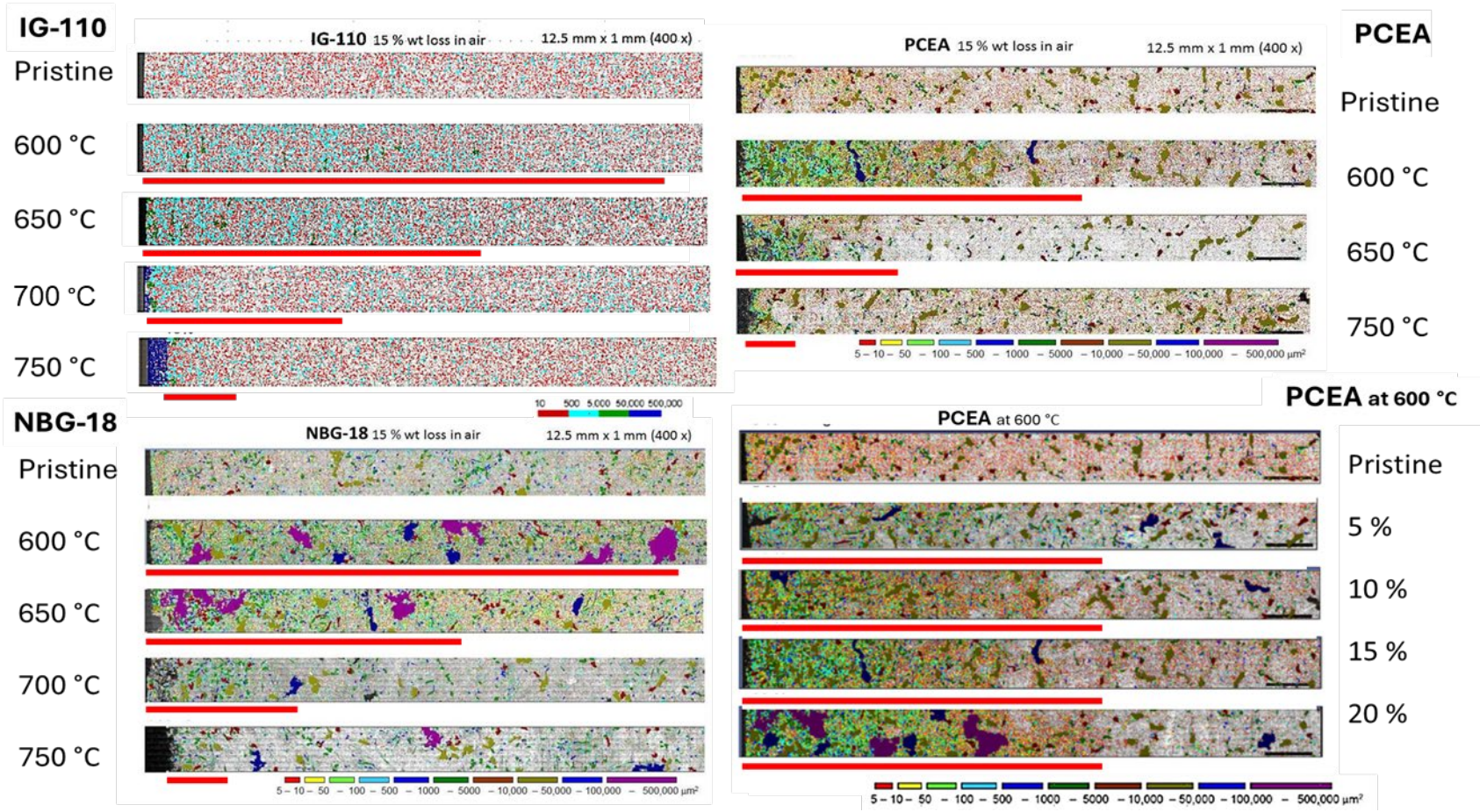

Fig. 5: Optical microscopy cross-section images (400×) of oxidized graphite to 15 % WL at various temperatures (IG-110, NBG-18, PCEA) and at various WL levels at constant temperature (PCEA at 600 °C). Pores are color-coded based on their size. The optical fields are 12.5 × 1 mm^2 in all images. The maximum length of active oxidation zone in each image was identified visually from these images and cross-validated by pixel intensity profiles in the direction of oxidant penetration (from left to right in these images). Results are presented in Table 2. (Data adapted from refs. [17,47,50].)

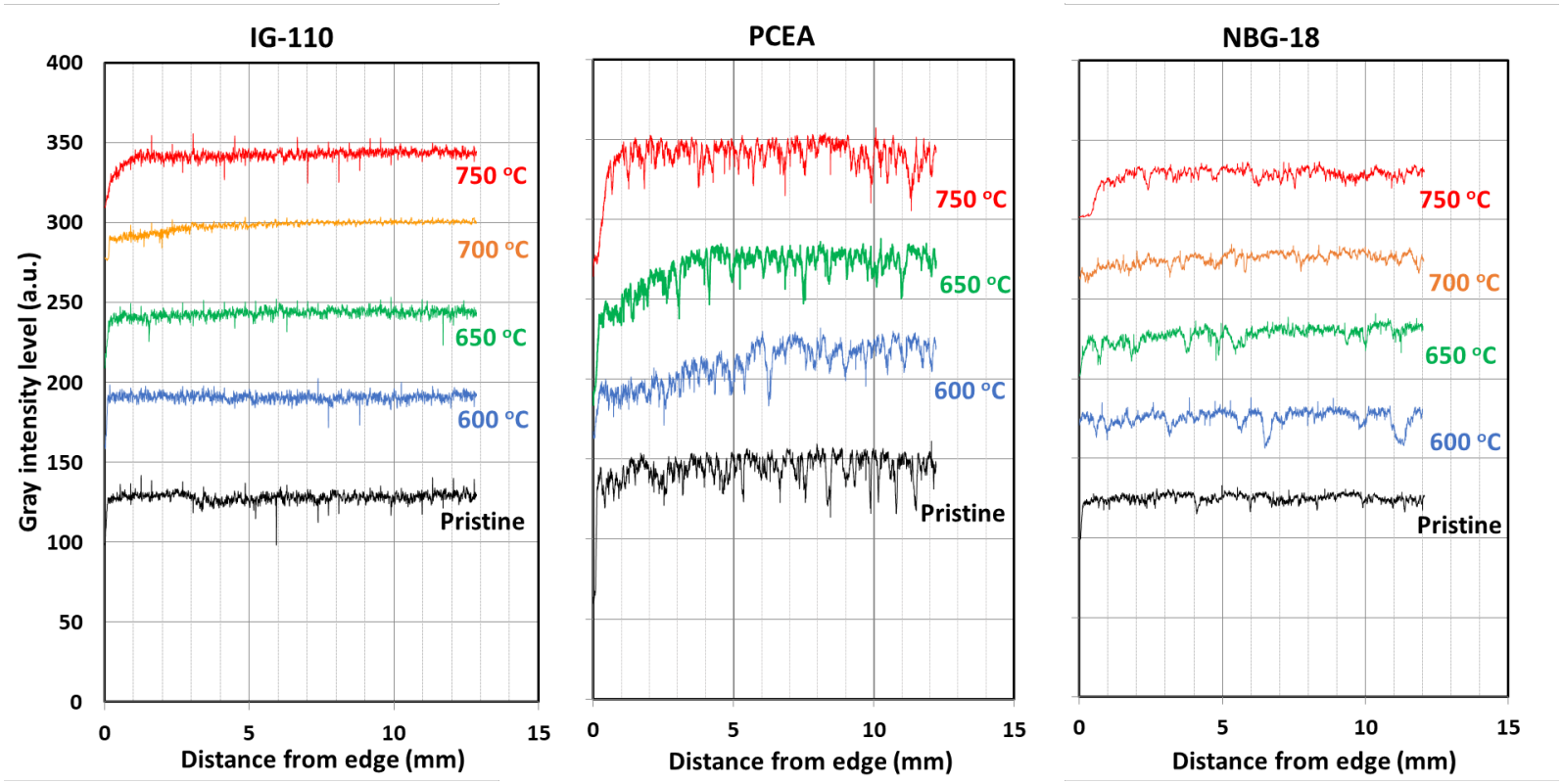

Fig. 6: Area-averaged pixel intensity profiles images as a function of radial distance from the exposed surface in cross-sectioned graphite specimens oxidized to 15 % WL. The constant temperature traces have been shifted upwards by 50 units increments to avoid their overlap. The vertical scale represents pixel brightness intensities on a scale between 0 (extreme black) and 255 (extreme white). Low reflecting spots (porosity) appear darker (lower pixel intensities) than polished graphite surfaces (higher pixel intensities). The width of each trace's curved zone near the surface (edge) indicates the thickness of the oxidized layer. The noise level differences between different graphites' profiles correlate with the grain size classification (fine / coarse grains) and the distribution of pre-existing pores. (Data adapted from refs. [17,47,50].)

6.3. First Results

Figures 5 and 6 show significant differences between oxidation layers of the three graphite grades, but the trend of oxidized zone shrinking with the increase of oxidation temperature is common. Oxidation at the highest temperatures (700 – 750 °C) causes clear surface corrosion, accompanied by dimensional reduction. The development of active oxidation zone with the increase of total WL is shown for PCEA at 600 °C (Fig. 5). A systematic comparison of pixel intensity profiles at three temperatures and various WL levels is presented in Fig. B1 of Appendix B. As discussed elsewhere [22,47,50], fast oxidant transport through the network of interconnected large pores generates new narrow pores in the binder, which has lower oxidation resistance. As the WL increases, large pores near the surface continue to grow and finally merge in large voids, whereas near the maximum penetration depth, fine pores continue to multiply. These observations support the Wichner model's assumption that isothermal oxidation occurs via multiplication of fine pores and growth of larger pores within subsurface zone of constant length.

Together, Figs. 5, 6 and B.1 support the same conclusions: (1) penetration depth length depends primarily on the oxidation temperature; (2) increasing the WL level at constant temperature enhances local oxidation in the subsurface zone but does not enlarge penetration lengths; (3) each graphite grade's behavior of depends strongly on its microstructure.

Figure 7 compares the evolution of volume and density of oxidized IG-110 and PCEA samples [53,54]. The temperature effect is evident for IG-110 specimens oxidized to 15 % WL. Bulk (uniform) oxidation in Regime 1 at 600 – 650 °C decreases the density, but the volume remains constant. By contrast, nonuniform oxidation in Regime 2 (700 °C) and transition to Regime 3 (750 °C) occurs with gradually increasing density (though never reaching that of the unoxidized graphite) and continuous volume reduction. Bulk oxidation of PCEA at 650 °C maintains constant volume, whereas density decreases gradually with increasing WL. Oxidation at 750 °C in the same WL range produces lower values of both density and volume.

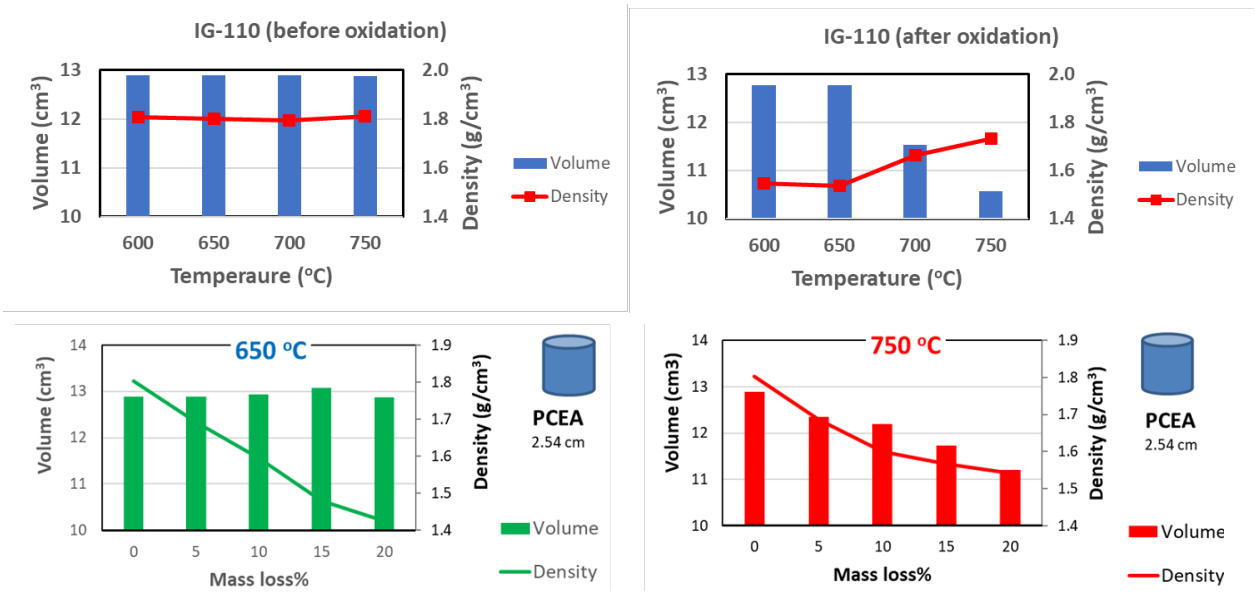

Fig. 7: Typical volume and apparent bulk density evolution of graphite specimens (Ø = *h* = 25.4 mm) after oxidation. Top row: IG-110 graphite oxidized to constant WL (15 %) at different temperatures. Bottom row: PCEA graphite oxidized at two temperatures and increasing WL levels. (Author's data recalculated from refs. [53,54].)

Table 2 shows maximum penetration depth for fully developed oxidized layers and their respective oxidation temperatures based on visual observations and pixel intensity profiles from optical microscopy data [17,22,47,50,53] and density profile measurements at Oak Ridge National Laboratory [16,50]. Additional information from other sources on oxidized layer structures of IG-110 [18,31,46,54] and NBG-18 [18,52] is included for comparison. Details are available in Appendix C. Also included are calculated results for maximum penetration length of O_2 in IG-110 machined as spherical pebbles [55].

Table 2: Maximum penetration depth of oxidized layers of graphite specimens oxidized in air at various temperatures.

NBG-18			PCEA			IG-110			R4-650		
Temp. °C	Depth mm	Ref.	Temp. °C	Depth mm	Ref.	Temp. °C	Depth mm	Ref.	Temp. °C	Depth mm	Ref.
600	11.93	[17]	600	7.45	[22,50]	550	~25.00	[31]	600	8	[16]**
650	7.07	[17]	650	3.56	[22.50]	600	11.68	[47,50]	650	4.3	[16]**
700	3.40	[17]	700	1.60	[17]*	600	12.5	[55]	650	5.8	[16]***
700	3.31	[18,52]	750	1.09	[22.50]	650	7.58	[47,50]	700	2.2	[16]**
750	1.63	[17]				650	8.50	[31]	700	1.7	[16]***
						700	4.38	[47,50]	750	1.1	[16]***
						700	>5.00	[18,54]			
						700	5.00	[55]			
						750	1.63	[47,50]			
						800	2.50	[55]			
						800	1.10	[46]			

*Nonstandard dimensions specimen (Ø = 12.5 mm; h = 25.4 mm) oxidized to 15 % WL
**Low WL range (15 –20 %)
***High WL range (35 –77 %)
Note: Much of the data in this table were measured by optical microscopy of standard-size specimens (Ø = h = 25.4 mm) oxidized to 15 % WL according to ASTM D7542 [16,17,22,47,50].

7. FINDING THE STRUCTURE FACTOR

Data in Table 2 show estimates of maximum penetration depth of graphite specimens oxidized at various conditions. Although the "maximum" depth of the oxidized layer can be identified only with some approximation (see section 6.2), its variation with temperature is clear and significant. Using the above definition of maximum penetration depth, X_δ, where $\delta = C(X_\delta)/C_0 = 0.01$, Eq. (8) can be rewritten as follows:

$$X_{0.01} = -\ln(0.01)\sqrt{\frac{\beta D_0(T)}{A(T)}}. \quad (9)$$

By this definition, $X_{0.01}$ is the distance at which only 1 % of surface oxygen is still available for oxidation, and the local graphite density is 99 % of the unoxidized bulk density. Because the temperature variations of free gas oxygen diffusivity (D_0) and of reactivity (A) factors are both

known, this simple relationship can be used to estimate β by conducting a regression analysis for each graphite grade. The results for variation of $X_{0.01}$ with temperature (Table 2) are shown in Fig. 8 along with the corresponding β values (also listed in Table 1).

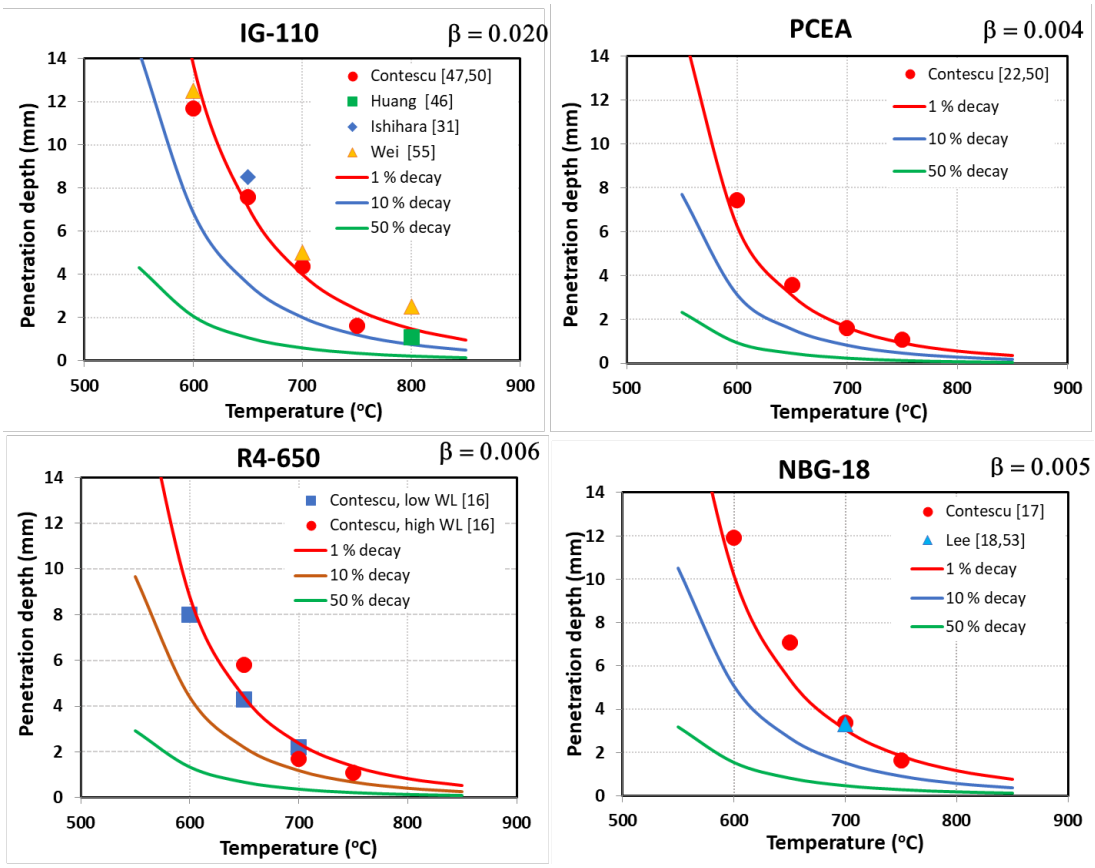

Fig. 8: Experimental data for temperature effect on the distance $X_{0.01}$ from the surface, corresponding to residual oxygen concentration of 1 % from surface concentration, equivalent to 1 % density decay from the bulk graphite density. The values of β obtained by linearization of experimental data are shown for each grade. Projections for $X_{0.10}$ and $X_{0.50}$ (i.e., 10 % and 50 % density decay) are also shown for comparison.

Fig. 9 shows calculated oxidant concentration ratios relative to the surface concentration as a function of distance from the surface and of temperature. These data were calculated using Eq. (8) with the graphite-specific structural parameters β in the diffusivity term, and the Arrhenius kinetic parameters (Table 1) in the reactivity term from Eq. (2). As the oxidation temperature

increases, the maximum oxidant penetration becomes narrower and more restricted near the surface.

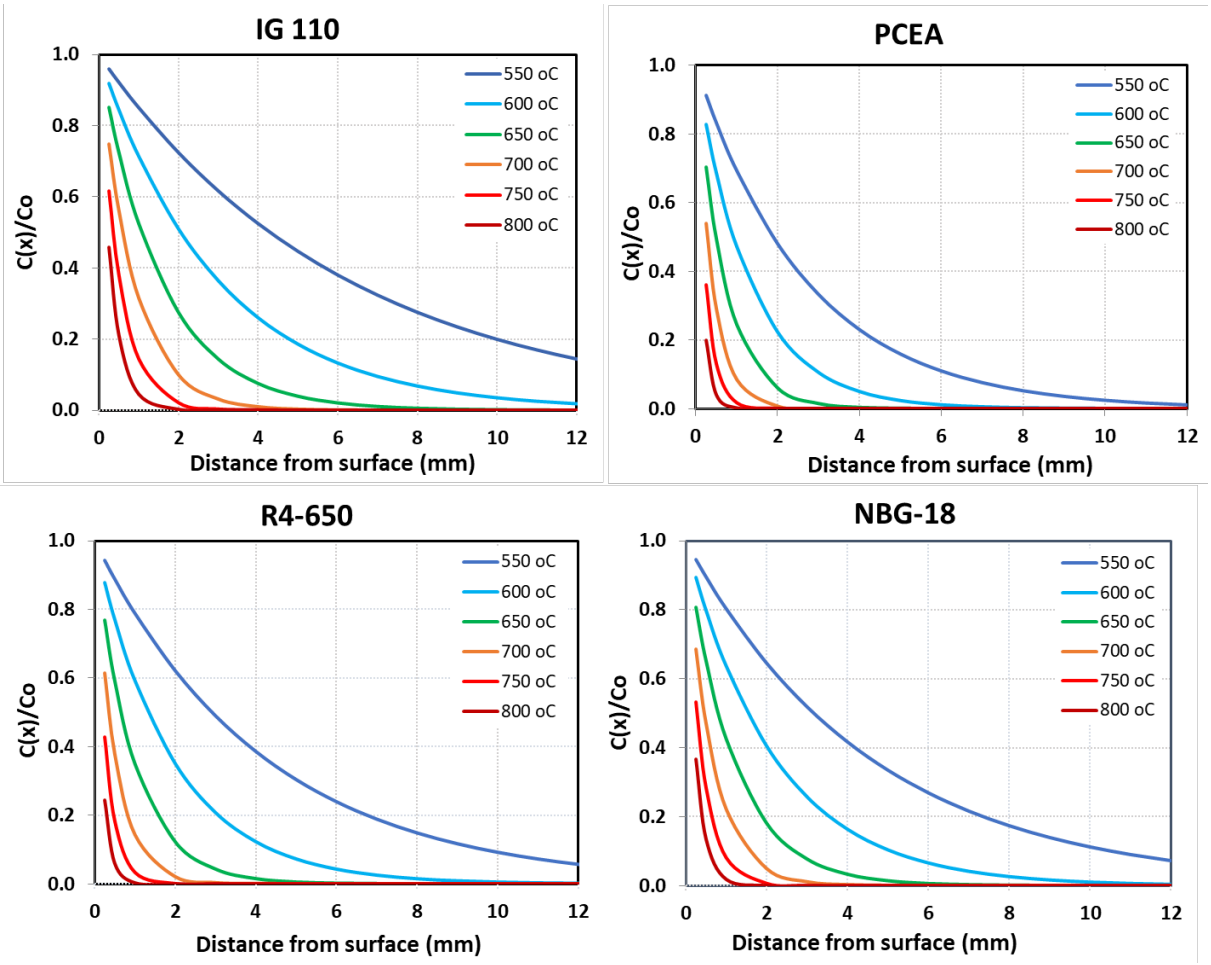

Fig. 9 Temperature effect on distribution profiles of residual oxygen fraction relative to its surface concentration.

Figure 10 shows calculated density profiles corresponding to fully developed oxidized zones at several temperatures. These data were calculated by introducing β coefficients previously obtained in Eq. (8) along with the appropriate temperature variation of reactivity from Eq. (2) and diffusivity from Eq. (4) for each graphite grade (Table 1). Where experimental ρ_0 values were not available, they were replaced by zero. Microstructural differences between graphite grades influence the evolution of specific density profiles with temperature. At equal oxidation temperatures, the width of the oxidized layer decreases in the order IG-110 > NBG-18 > R4-650 > PCEA, which is also the order of β coefficients. An independent confirmation of the

model presented here is available for graphite NBG-18 [18,52]: the density profile predicted for oxidation at 700 °C agrees with the density profile reported by Lee et al. for NBG-18 graphite oxidized up to about 10 % WL at the same temperature.

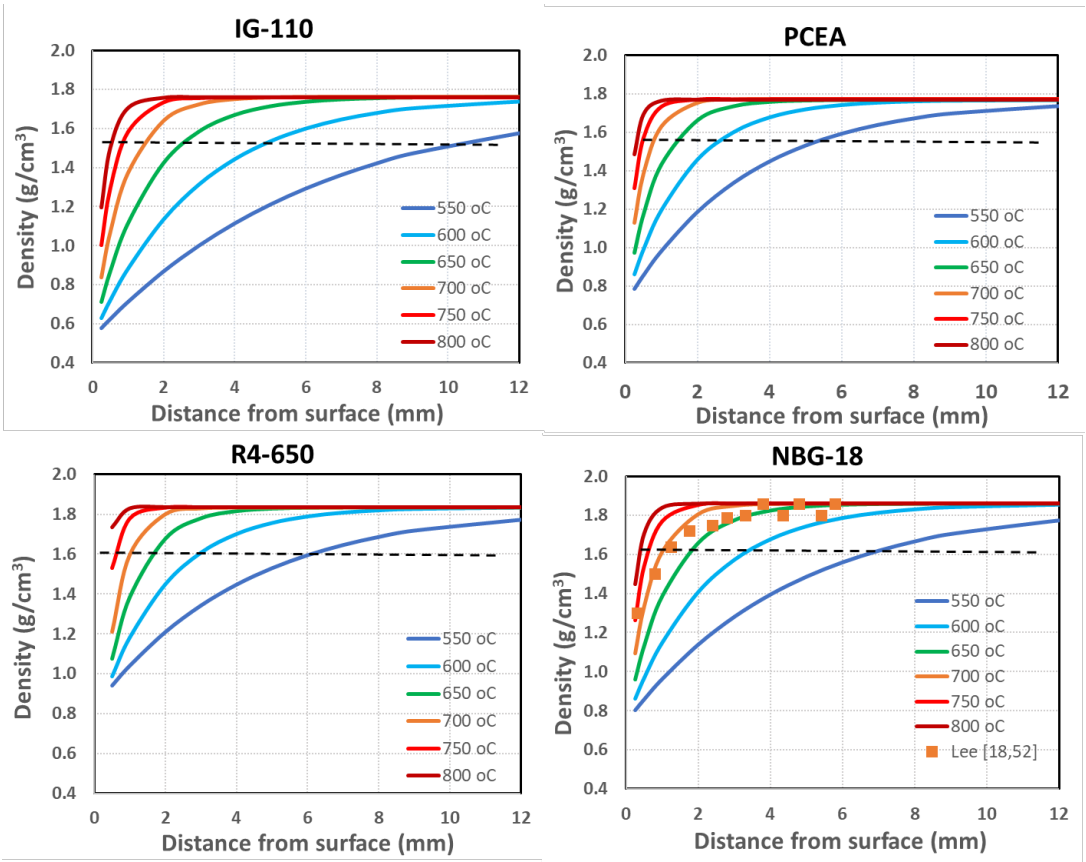

Fig. 10: Estimated graphite density profiles at various oxidation temperatures. Data points reported by Lee [18,52] for the density profile of NBG-18 oxidized at 700 °C match very well the profile calculated at that temperature. Dotted lines show the 10 % density decline levels for each grade.

The density profiles measured by the lathing method for graphite R4-650 oxidized at three temperatures and two levels of WL (Table 2) have been reported elsewhere [16]. The original information available in Fig. C.4 of Appendix C is now compared with the present model predictions. The calculated density profiles for two series of specimens corresponding to 15 % < WL < 19 % and 35 % < WL < 45 % are shown in Fig. 11. For these samples, the density ρ_0 of the very first surface layer (< 1 mm thin) was available from direct measurements, and the

ratio ρ_0/ρ_∞ was used in Eq. (7) for a more accurate representation of density profiles. The ρ_0/ρ_∞ ratios were 0.4, 0.3, and 0.1 for the low WL samples oxidized at 600, 650, and 700 °C. In this group, the calculated density profile fits the experimental data quite well, except for the sample oxidized at 600 °C, where the agreement is partial. We do not have a satisfactory explanation for the difference.

In the group of high-WL specimens, the ratios were 0.15 at 650 °C and 0.05 at 700 and 750 °C. Moreover, the intense corrosion of high-WL specimens—namely 3, 4.2, and 1.1 mm in the radial direction at 650 °C (20 h), 700 °C (8 h), and 750° C (1.5 h)—was also accounted for. With this information, the calculated profiles describe experimental profiles at each temperature very well. One notable exception is the sample oxidized for 70 h at 600 °C to 40 % WL. As previously reported [16], these conditions led to total penetration and massive bulk oxidation. This oxidized specimen was the only one that did not have a central region with density close to that of the unoxidized graphite.

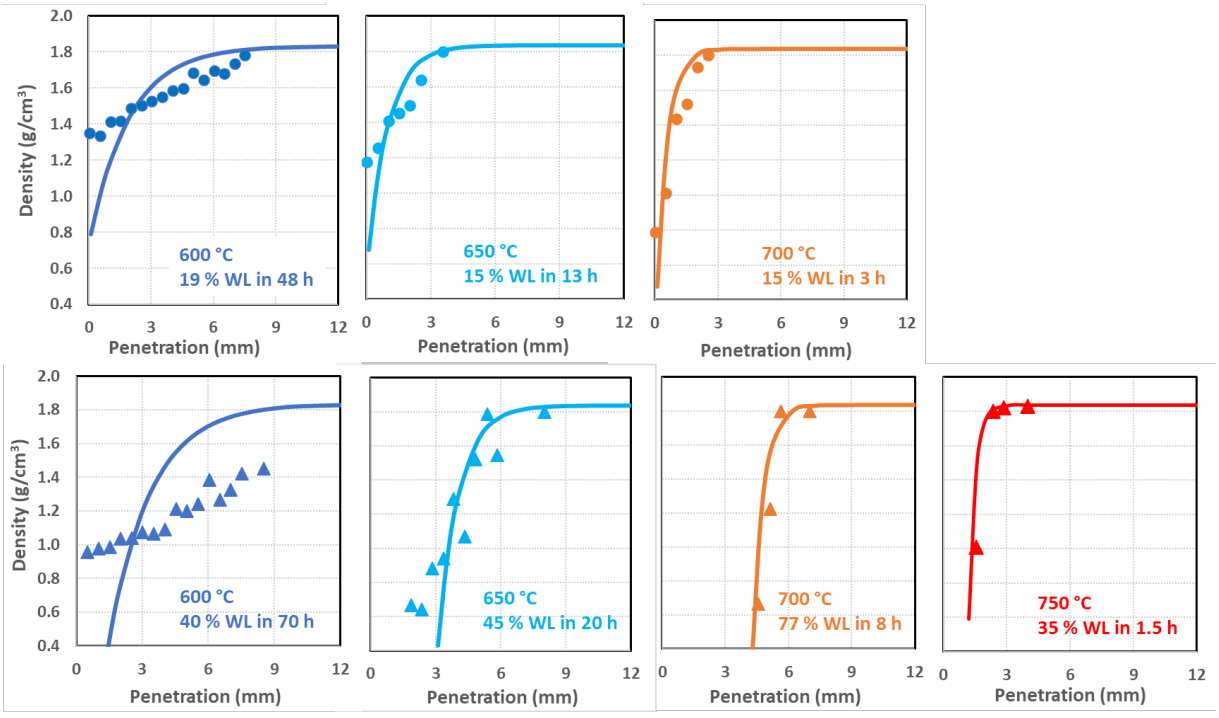

Fig. 11: Comparison of density profiles calculated using Eq. (5) vs. profiles measured by the lathing method for graphite R4-650 oxidized at various temperatures and WL levels. (Adapted from ref. [16].)

Similar behavior was observed after oxidation up to about 10 % WL of 12.4 mm cubes of graphite IG-110 at 700 °C. Measurements reported by Lee [18,54] indicated that densities increased from 0.6 g/cm^3 near the surface to 1.2 g/cm^3 close to the center but never reached the density of unoxidized graphite (1.76 g/cm^3). Original results are illustrated in Fig. C.3 in Appendix C. Reliable analysis could not be conducted for these data because the graphite specimens used in the experiment were too small. Obviously, the simplified model presented above meets its limits of applicability in conditions of bulk oxidation combined with dimensional reduction. Nevertheless, Fig. 11 demonstrates how the unique graphite-specific coefficient β can be used, in conjunction with the reactivity (A) and free gas diffusivity (D_o) values at each temperature, to describe density profiles at various oxidation conditions in good agreement with the experimental observations.

8. DISCUSSION

The opposite temperature trends of reactivity and diffusivity terms in Eq. (1) cause large variations in penetration depth in the subsurface region affected by oxidation: from tens of millimeters at low temperatures to about 1 mm or less at high temperatures (Figs. 4 - 6). Apparently, low-temperature oxidation causes more widespread damage in graphite than oxidation at high temperatures, but this conclusion is only partially correct because the oxidation rate factor was not yet accounted for. A full representation of temperature effects on oxidation is available in Fig. 12 for each graphite grade. This figure compares logarithmic plots of penetration depths and oxidation rates vs. oxidation temperature. From 600 °C to 750 °C the rates *increase* by more than two orders of magnitude, whereas penetration depths *decrease* by less than one order of magnitude. Deep oxidation of standard–sized specimens [40] at 600 °C takes tens of hours to reach 15 % WL. By contrast, at 750 °C, the same 15 % WL target is reached in only 1 or 2 h (Fig. 3). If high-temperature oxidation continues for longer times, then the fast surface corrosion process continues, and the narrow surface-limited corrosion zone moves inward, causing rapid changes in the shape and dimensions of graphite specimens.

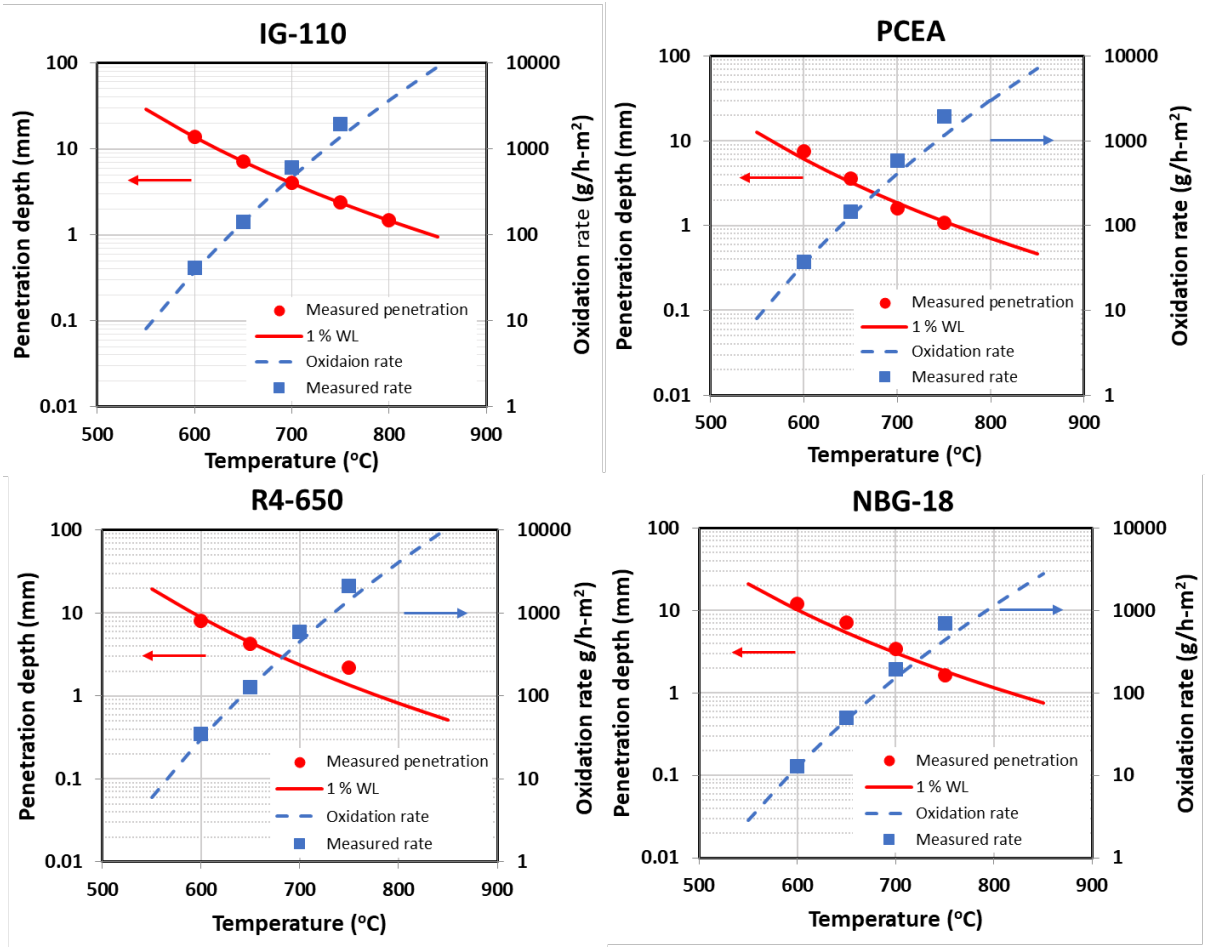

Fig. 12: The opposite trends of oxidation penetration depth (mm) and oxidation rates (g h^{-1} m^{-2}) as a function of temperature.

In practice, brief exposure of graphite components to air at low temperatures after a hypothetical air ingress will have less significant effect on physical integrity compared with equal-time exposure at higher temperatures. In the former case, deep penetration of oxidation under the surface would enlarge the oxidized layer and reduce the gradient of mechanical strength decay; the oxidation process would advance slowly, and the damage would be restricted, especially if the amount of oxygen is limited [27]. Analysis of such DBE air ingress accident scenarios showed that if only a limited amount of oxygen has breached the helium pressure barrier, then it would be quickly consumed by the huge graphite mass in the reactor, and the surface damage would be less than 1 mm [28]. However, if the air ingress accident is not mitigated quickly and air has access to high-temperature components in the lower plenum, then surface corrosion in Regime 3 (a BDBE postulated scenario) might rapidly produce dimensional changes, possibly compromising the reactor's support columns' buckling strength [56,57].

Increased porosity upon oxidation lowers the density and reduces the strength (and other density-related properties) of oxidized graphite. These changes are localized, and their magnitude varies exponentially with the distance from the exposed surface. To correctly evaluate the relationship between mechanical properties (compressive and tension stress, elastic modulus) and oxidation effects, these properties must be measured on homogeneous samples (i.e., on uniformly oxidized specimens) that are as free as possible of density gradients. Bulk-oxidized (or "uniform") graphite samples can be recognized by their lower density and constant volume (Fig. 7). Uniformly oxidized graphite samples can be obtained by slow oxidation of laboratory-size specimens (e.g., cylindrical rods) at low temperatures when oxidation is in Regime 1. Because of slow oxidation rates, the target WL levels will take a long time to reach, but oxidation will spread uniformly in the bulk. Such measurements were published for graphite IG-110 (or its early version, IG-11). Fig. 13 shows a collection [58] of compressive strength data measured on thin (diameters not larger than 10 – 12 mm) specimens, oxidized slowly in air at 450 – 550 °C [59,60,61,62,63] or in mixtures containing H_2O or CO_2 and an inert gas at 750 – 850 °C [59]. The data scatter is unavoidable because of aleatory nonuniformity of graphite materials, but the regression analysis on all 127 data points led to the following relationship between compressive strength reduction and the WL of uniformly oxidized samples:

$$\frac{\sigma}{\sigma_0}_{\text{broad range}} = \exp(-0.056\ \text{WL\%}); \quad R^2 = 0.917. \tag{10}$$

If only data from a narrower range (WL < 10%) were considered, then a more aggressive strength loss relationship is obtained:

$$\frac{\sigma}{\sigma_0}_{\text{narrow range}} = \exp(-0.073\ \text{WL\%}); \quad R^2 = 0.894. \tag{11}$$

Similar relationships have been found empirically by Knudsen [64] for brittle polycrystalline materials and were later generalized [65] to describe the decline of flux-related properties (tension and compressive strength, Young's modulus, thermal conductivity) with the increase of porosity fraction in graphite and other crystalline materials.

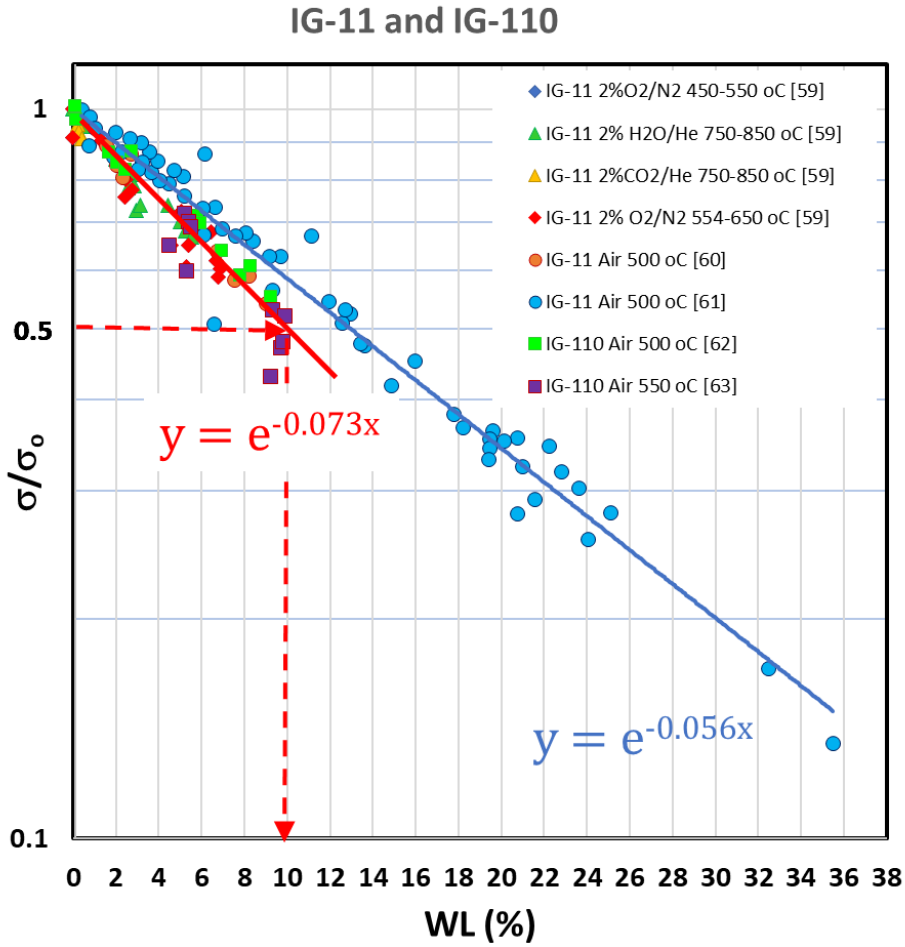

Fig. 13: Reported data [59,60,61,62,63] on compressive strength loss of uniformly oxidized graphite IG-11 and IG-110 as a function of WL. (Adapted from ref. [58].)

For specimens uniformly oxidized (at constant volume), the measured WL generally corresponds to density loss fraction. Therefore, Eq. (11) can be rewritten:

$$\frac{\sigma}{\sigma_0} = \exp\left[-0.073\left(1-\frac{\rho}{\rho_\infty}\right)\times 100\right]. \qquad (12)$$

By contrast, the temperature dependence of density ratio ρ/ρ_∞ can be calculated from Eq. (7); if ρ_0 is not known, then it may be neglected. The evolution of IG-110 density profiles as a function of oxidation temperature is shown in Fig. 14a. Using the correlation from Eq. (12), the evolution of compressive strength profiles vs. oxidation temperature is plotted in Fig. 14b.

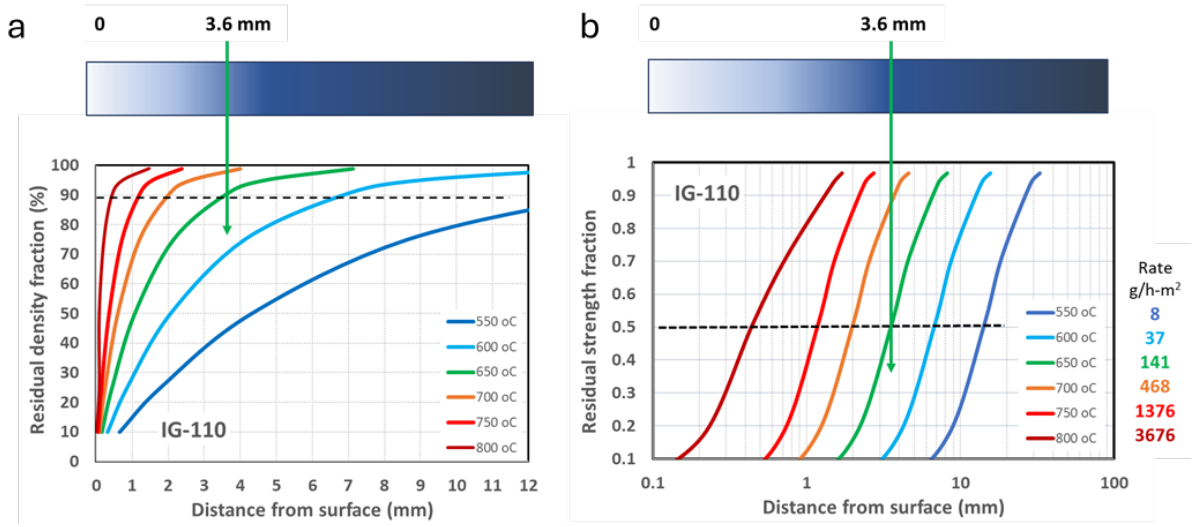

Fig. 14: Temperature effects on density profile and compressive strength profile in fully developed oxidized zone predicted for oxidized IG-110 graphite. Also indicated are the calculated oxidation rates (g h^{-1} m^{-2}) at these temperatures. In the example shown for 650 °C oxidation temperature, 10 % WL and the corresponding 50 % strength loss occur at 3.6 mm from the exposed surface.

The two plots in Fig. 14 contain information that might be useful for analysis of oxidation effects in the design phase. In this example, the design-specific calculations were assumed to indicate that the compressive stress failure limit for an IG-110 graphite component occurs at $\sigma/\sigma_0 < 0.5$. Data on uniformly oxidized specimens (Fig. 13) show that this level of compressive strength decay occurs at $\rho/\rho_\infty < 0.9$, or >10 % global WL. These thresholds are represented by dotted lines in Fig. 14. Considering oxidation at 650 °C of a large graphite body as an example, 10 % local weight loss (Fig. 14a) and 50 % strength decay (Fig. 14b) would occur at 3.6 mm from the surface. In this example, the suggested dimensional allowance for the (relatively slow) oxidation at 650 °C is 3.6 mm. At higher temperatures, the 10 % density reduction and 50 % strength decay limits are narrower: 2 mm at 700 °C and 1.2 mm at 750 °C. However, *much faster* oxidation rates at these temperatures would *rapidly* produce surface corrosion and dimensional changes. The information on density and strength profiles should always be paired with kinetic analysis (Fig. 12). At low temperatures, the model shows that *fully developed* oxidized zones are large (e.g., 28.6 mm at 550 °C and 7.1 mm at 650 °C for the fine-grained IG-110 graphite), but the oxidation rates are relatively slow (e.g., 8 and 141 g $h^{-1}m^{-2}$, respectively). Limited oxidation at these temperatures is not expected to produce structural damage if the air leakage is stopped

quickly [28]. High-temperature oxidation has more severe effects. *Fully developed* oxidized zones are narrower (e.g., 2.4 mm at 750 °C, 1.5 mm at 800 °C; Fig. 8), and the excluded oxidation regions based on the conservatively estimated strength vs. density relationship (Fig. 13) would be even narrower (about 1.2 and 0.4 mm, respectively; Fig. 14). However, much faster surface corrosion rates (about 1400 and 3700 g $h^{-1}m^{-2}$ at 750 °C and 800 °C, respectively) would cause rapid dimensional changes. They may lead to significant reduction in cross section and excessive stress, which would cause structure failure in a short time. These results could inform calculations involving severe air-ingress accidents. Similar estimates can be made for other oxidation temperatures, as deemed significant for other hypothetic scenarios. Moreover, similar plots can be derived for any other graphite grade when information on oxidation kinetics, effective diffusivity, and compressive strength becomes available.

One more important comment is necessary. Oxidation rates and the amount of carbon gasified cannot exceed the rates of oxidant supply and the total amount of oxygen that was leaked into the core. All kinetic information based on ASTM D7542 is obtained in conditions of excessive air supply rate, in which the rate of O_2 supply (mmol-O_2 min^{-1}) was at least 10 times higher than the fastest rate of carbon consumption (mmol-C min^{-1}) *at the highest oxidation temperature*. These testing conditions recommended by ASTM D7542 are required for decoupling kinetics from diffusion perturbations, so that kinetic information is unperturbed by diffusion effects. Published data on IG-110 oxidation using lower oxygen supply rates showed slower oxidation rates, and early transitions between Regimes 2 and 3, but reasonably stable activation energies [66,67,68]. Most air-ingress scenarios assume limited air supply, restricted by the natural convection of outside air in countercurrent with helium pressure discharge. Under these oxygen-starved conditions, oxidation rates may be significantly lower than the values indicated in Fig. 12. More experimental research and modeling are needed to correctly evaluate the graphite behavior under nonstandard oxidation conditions with limited oxygen supply.

9. CONCLUSION

The graphite-moderated reactor designer can benefit from the availability of a detailed graphite oxidation analysis procedure that can be used to evaluate oxidation effects on density profile and strength distribution in the subsurface of those graphite components. Chronic

oxidation effects are negligible, but oxidation caused by unlikely air-ingress events may significantly affect the functionality and integrity of graphite components. In the case of a more severe, but extremely unlikely, air-ingress scenario (BDBE) the affected graphite components would be damaged beyond repair, but their sacrificial oxidation would consume oxygen, thereby protecting the fuel. Modeling full-scale reactor behavior during such very low probability events is understandably affected by uncertainties related to the unpredictability of the triggering events. Correctly assessing the properties degradation of oxidized graphite components may involve some intractable variables that are hard to control. However, simulations that combine the effects of variable operational parameters, such as coolant chemistry, temperature, and local stress, can provide useful information for evaluating graphite components' reliability.

This article proposes an experiment-based method for estimating density- and strength-loss profiles in the subsurface of oxidized graphite components as a function of oxidation temperature. The procedure uses a simplified, but conservative, analysis of graphite oxidation and requires (1) standardized measurements of oxidation kinetics and estimation of reactivity parameters, (2) direct measurements of oxidant penetration depths (or density profiles) of *large* graphite specimens oxidized *nonuniformly* at several temperatures of interest, and (3) mechanical properties measurements on *small* graphite specimens oxidized *uniformly* at various WL levels. These three sets of information were used for graphite IG-110 as an example. Subsurface damaged regions in oxidized graphite were identified, and the effect of oxidation temperature on local profiles of density and strength was determined. The safety rules for design and construction of graphite-moderated reactors [3] recommend that these oxidation-damaged regions must be excluded from stress calculations and must be regarded as completely detached from the main body.

ACKNOWLEDGMENTS

This manuscript has been authored by UT-Battelle, LLC, under contract DE-AC05-00OR22725 with the US Department of Energy (DOE). The US government retains and the publisher, by accepting the article for publication, acknowledges that the US government retains a nonexclusive, paid-up, irrevocable, worldwide license to publish or reproduce the published form of this manuscript, or allow others to do so, for US government purposes. DOE will provide public access to these results of federally sponsored research in accordance with the DOE Public Access Plan (http://energy.gov/downloads/doe-public-access-plan).

APPENDICES

A. Graphite oxidation basics

Graphite oxidation by air is the result of several parallel processes: (1) oxygen diffusion into graphite, aided by the network of interconnected pores; (2) gasification reactions, in which oxygen chemically reacts with carbon atoms at internal pore surfaces and generates either CO_2 or CO (or both); (3) back diffusion of gas products to the free gas phase; and (4) microstructural changes in pore morphology and development of new pores owing to carbon loss. The general equation that accounts for the temperature-dependent stoichiometry of reaction products CO and CO_2 is written as follows:

$$[1 + 0.5\,f(T)]\ O_2 + [1 + f(T)]\ C = CO_2 + f(T)\ CO.$$

The stoichiometric coefficient for carbon, $N(T) = [1 + f(T)] / [1 + 0.5\,f(T)]$, and the reaction order for oxygen, $n = 1/N$, depend on the temperature-dependent molar ratio between the reaction products. We used the correlation compiled from various sources by Kim and No [67]:

$$f(T) = f_{CO/CO_2} = 7396 \exp\left(-\frac{69604}{RT}\right). \quad (A1)$$

The time-dependent global mass balance equation is obtained [19,39] by equating the rate of O_2 consumption from a gas volume element with the net sum of concentration changes caused by diffusion and chemical reactions:

$$\frac{\partial C}{\partial t} = \frac{1}{\partial x}\frac{D_{\text{eff}}}{\varepsilon}\left(\frac{\partial C}{\partial x}\right) - k_0 \exp\left(-\frac{E_a}{RT}\right) P^n F_b \frac{\rho}{\varepsilon} N(T). \quad (A2)$$

In this equation, C (mol/m^3) is the O_2 concentration in free gas and in graphite pores, x (m) is the distance from the exposed surface, and R and T are the gas constant and the absolute temperature. The graphite microstructural properties are characterized by the porosity fraction, ε (m^3-pores /m^3-graphite) and the molar density, ρ (mol C/m^3-graphite). The Fick's law diffusion term includes an effective diffusivity of the oxidant in graphite pores, $D_{\text{eff}} = \beta\, D_0$, where $\beta \ll 1$ is a microstructure-dependent factor representing the pore system impedance to oxidant transport, and D_0 is the O_2 diffusion coefficient in air; it varies proportionally with $T^{1.75}$ and inversely with

the total pressure. The term for chemical reaction rate follows Arrhenius' law, where k_0 (Pa^{-1} s^{-1}) and E_a (J/mol) are the frequency factor and the activation energy. Also included are the O_2 pressure, P (Pa), and a factor accounting for rate acceleration with the progress of oxidation, F_b. With the conservative assumptions $F_b = 1$ and $n = 1$ in this analysis (see below), k_0 is obtained from the pre-exponential factor of Arrhenius equation (using weight-normalized oxidation rates, OR_w, in s^{-1} units) divided by the free gas O_2 pressure. If area-normalized oxidation rates, OR_a, in g h^{-1} m^{-2} units, are used in the Arrhenius equation, the frequency factor would have different units (g Pa^{-1} h^{-1} m^{-2}).

Temperature strongly affects overall oxidation behavior. At any temperature, the slowest process between diffusion and chemical reaction controls the overall oxidation rate. At low temperatures, diffusion is much faster than chemical reactions, and the process is under chemical kinetics control (Regime 1). With increasing temperature, reaction rates follow the Arrhenius equation and increase exponentially, and the slower in-pore diffusion controls the process (Regime 2). At extremely high temperatures (and if sufficient oxidant supply is available), chemical rates become so fast that the oxidant is consumed as soon as it crosses the stagnant boundary layer at the exposed surface (Regime 3). At these extreme conditions, very fast gasification at the exposed surface causes graphite corrosion accompanied by dimensional and geometrical shape changes.

Perfectly uniform oxidation profiles cannot be obtained, even in Regime 1, because of the ever-present competition between diffusion and reaction rates. The unbalanced temperature variation of these two processes (i.e., $T^{1.75}$ vs. $\exp(-1/T)$, respectively) generates temperature-dependent gradients of oxidant concentration and of graphite density. With the increase of physical dimension of graphite blocks, the weight-normalized rates (wt %/min) decrease because large internal volumes remain unoxidized. This observation supports the concept of an "active oxidation zone" [14]. Oxidation of large graphite blocks, such as moderator elements or support posts, occurs within a temperature-dependent thickness, $\Delta h = \Delta h(T)$ near the surface, except in very early oxidation stages and situations in which Δh is larger than half the characteristic dimension of the graphite parts.

In the oxidation model proposed by Wichner [19,39], $\Delta h(T)$ is calculated from the temperature variation of chemical-reaction and oxidant-transport rates. Evidence shows that,

even with a few simplifications, the model is viable and can be used to guide estimation of temperature effects on density distribution in oxidized graphite components.

The following is a simplified version of Eq. (A2), which can be solved analytically:

$$\frac{\partial C}{\partial t} = \frac{\beta D_0}{\varepsilon}\frac{\partial^2 C}{\partial x^2} - \frac{A(T)}{\varepsilon}C, \qquad (A3)$$

where *A(T)* is the reactivity term, given by

$$A(T) = k_0 \mathrm{R}T \exp\left(-\frac{E_a}{\mathrm{R}T}\right)\frac{\rho}{\varepsilon}F_b N(T). \qquad (A4)$$

The R*T* factor is needed for expressing oxidant partial pressure in convenient concentration units in eq (A2). The unknown coefficient β in the diffusivity term can be found from analysis of experimental data. A quasi-steady state is assumed when $t \to \infty$ and $\partial C/\partial t = 0$, which leads to

$$\beta D_0 C'' + AC = 0. \qquad (A5)$$

Introducing

$$B^2 = \frac{A}{\beta D_0}, \qquad (A6)$$

the steady-state solution is obtained as

$$\frac{C(x)}{C_0} = \exp(-Bx) = \exp\left(-x\sqrt{\frac{A}{\beta D_0}}\right), \qquad (A7)$$

with boundary conditions $C(x = 0) = C_0$ (constant free gas oxidant concentration at the surface, $x = 0$) and $C(x \to \infty) = 0$ (no oxidant at very large distance). The result shows that the oxidant concentration profile at steady state decays exponentially with the distance, and the decay rate *B* depends on the ratio between the reactivity term *A* and the effective diffusivity term, $D_{\mathrm{eff}} = \beta D_0$. The gradient of oxidant concentration generates a reverse variation of graphite density, which increases from a remnant low value at the surface, ρ_0, to the bulk value ρ_∞ at some finite distance $\Delta h(T)$. By convention, the depth of maximum oxidant penetration is defined as the distance X_δ from the surface, where $C(x)/C_0 = 0.01$. At that distance, the local weight loss is 1 %, and the local density is 99 % of the bulk density.

A few simplifications were used to allow analytical solutions:

(i) Linear oxidation kinetics (i.e., $n = 1$). This approximation is conservative because setting the reaction order for oxygen at a higher value ($n = 1$) than what has typically been reported from kinetic measurements ($n \approx 0.7$) increases the effect of P_{O2} and gives faster oxidation rates.

(ii) Constant graphite microstructure (i.e., neglecting moderate variations of ρ, ε, and β, as proposed in an early graphite design document [69]). Measurements on British pile graphite oxidation indicated average values for β of about 0.01, in agreement with this work's results. However, β values had a modest linear increase with the oxidation progress (e.g., from 0.008 initial value to 0.03 at 10 % WL and to 0.07 at 20 % WL) [43,70]. Exact measurements for the new grades of graphite before and after oxidation by air require specialized equipment [45,71] and have not been reported.

(iii) Fully developed oxidation process (i.e., $F_b = 1$). The increase of F_b in the initial oxidation phase (up to, approximately, 5 % WL) can be evaluated by using random pore models with one [72] or two [73] empirically fitted constants. Experimental results for modern nuclear graphites indicate that reaction rates measured at 10 % WL are about 3.5× (NBG-18), 5× (IG-110), and 9× (PCEA) faster than near 1 % WL [58]. However, the Arrhenius factor k_0 is already compounded with the maximum value of F_b because the reaction rates calculated [40] between 5 % and 10 % WL are faster than in the early oxidation stages (Fig. 3). As demonstrated elsewhere [58], oxidation rate measurements adhering to ASTM D7542 are reproduceable between different laboratories and provide consistent values of the kinetic parameters E_a and k_0. Being derived from the WL range in which oxidation rates are the highest, these parameters are conservative and represent more severe behavior than at early oxidation stages.

B. Pixel intensity profiles in SEM images of graphite PCEA oxidized at various temperatures and weight loss levels

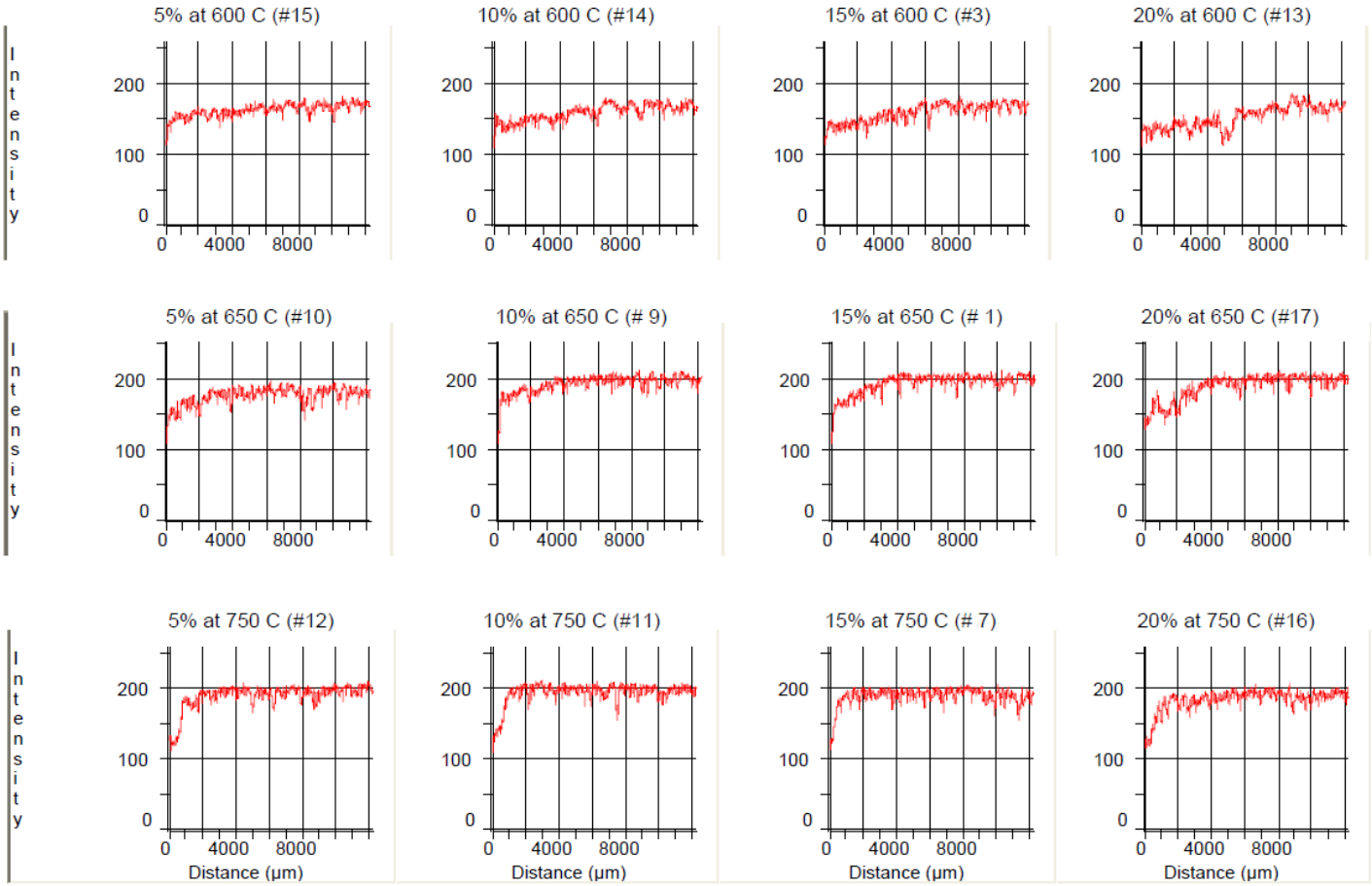

Fig. B.1 Radial pixel intensity profiles in the oxidized layer of PCEA graphite showing the radial distribution of pore densities. Pixel values between 0 (extreme black) and 255 (extreme white) are plotted as a function of the distance (in μm) from the exposed surface. Oxidized layers with high pore densities are indicated by small pixel values near the specimens' edges. (Data from ref. [17]).

C. Literature results on penetration depth in oxidized graphite

This section shows additional information from independent sources that analyzed the structure and evaluated the thickness of surface graphite layers after oxidation in air at specific conditions. This information was appropriately cited in the main text but is provided here with more pertinent details paraphrased from the original sources.

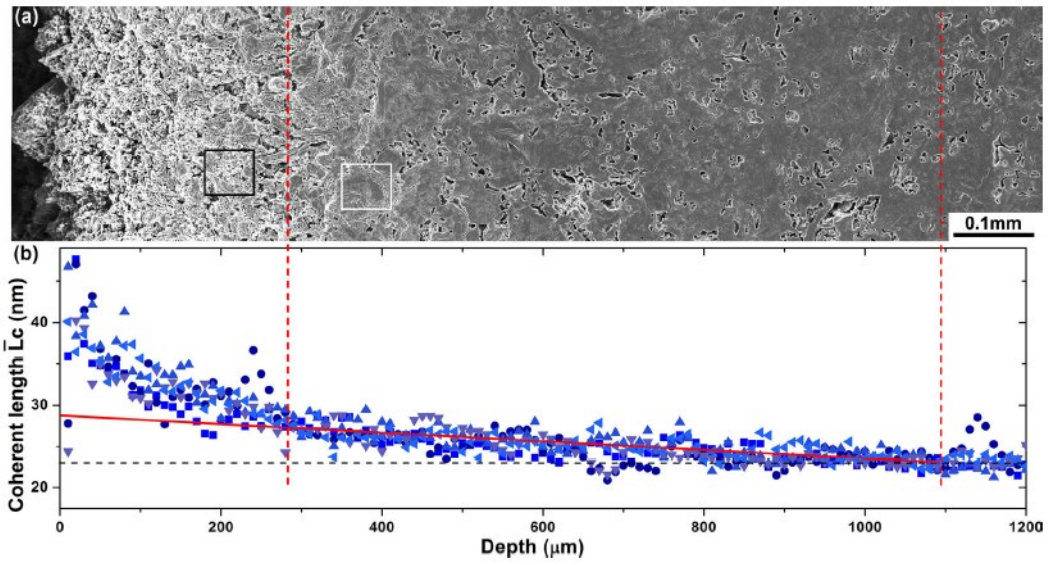

Fig. C.1 Cross section of an IG-110 specimen oxidized at 800 °C in air for 1.5 h up to 12.3 % WL. The top figure (a) shows mosaic scanning electron microscopy images at 500× magnification with 74 nm resolution. The bottom image (b) shows the profile of average coherent length L_c for the <c> direction. A thin (280 mm) remnant oxidized layer survives at the surface with a loose structure but higher coherent L_c lengths, which are caused by stronger contributions from filler crystallites after removal of less graphitized binder particles. The end of the oxidized layer (1100 mm) was identified from micro-X-ray analysis based on profiles of (002) peak intensity, broadening, and position in the subsurface layer. (Reproduced from ref. [46] with permission.)

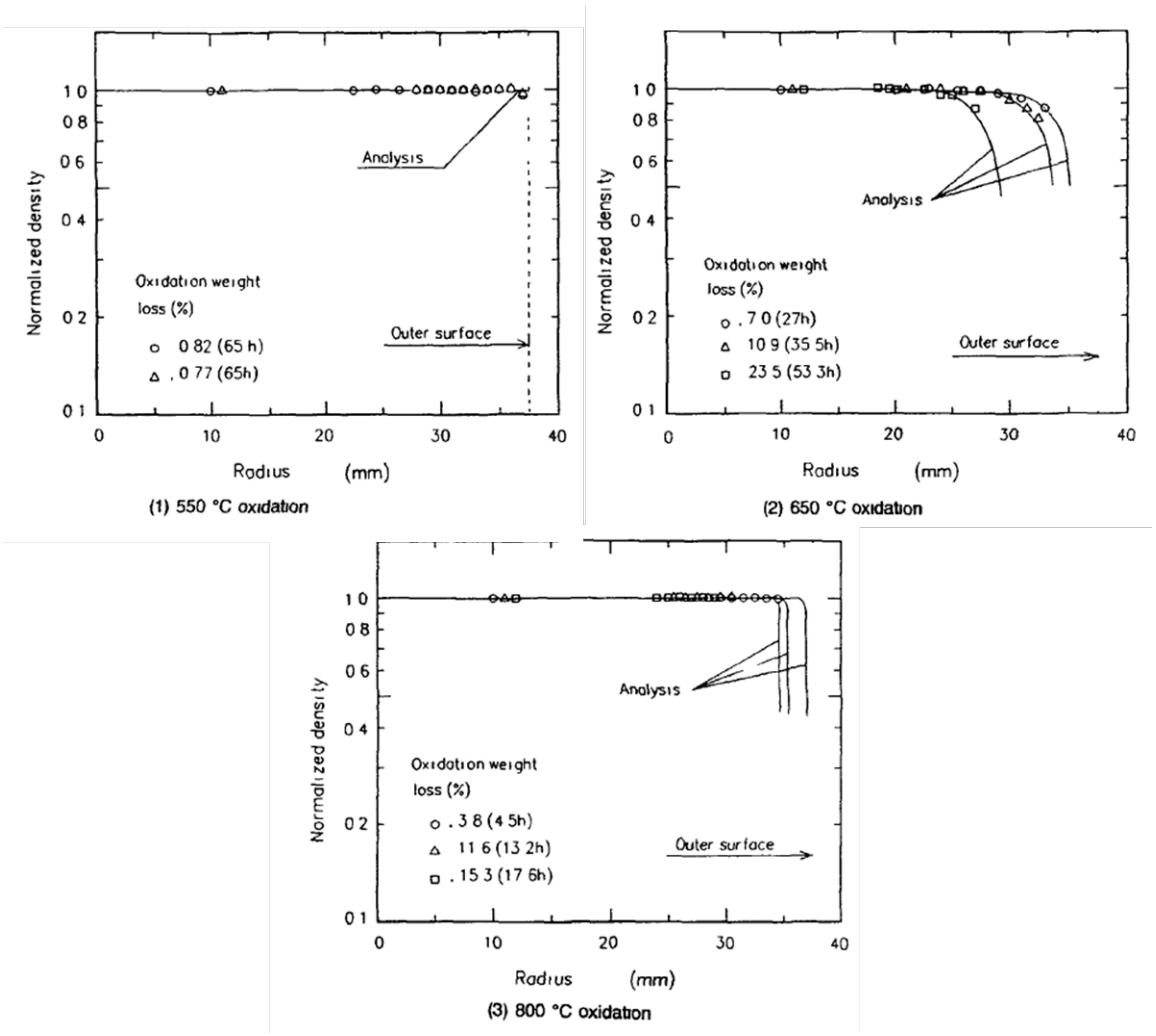

Fig. C.2 Density variation in subsurface regions of graphite IG-110 oxidized at three temperatures and various WL levels. Density profiles were obtained using the lathing procedure. Density profile results based on post-experiment data analysis are shown along with the corresponding WL levels and oxidation times, in parallel with dimensional reduction after oxidation in Regime 2. Slow oxidation at 550 °C produced uniform oxidation in a 25 mm subsurface zone (Regime 1). Development of oxidized layer profiles and slow dimensional reduction (Regime 2) are observed at 650 °C. Fast corrosion with significant dimensional reduction (Regime 3) is observed at 800 °C. (Reproduced from ref. [31] with permission.)

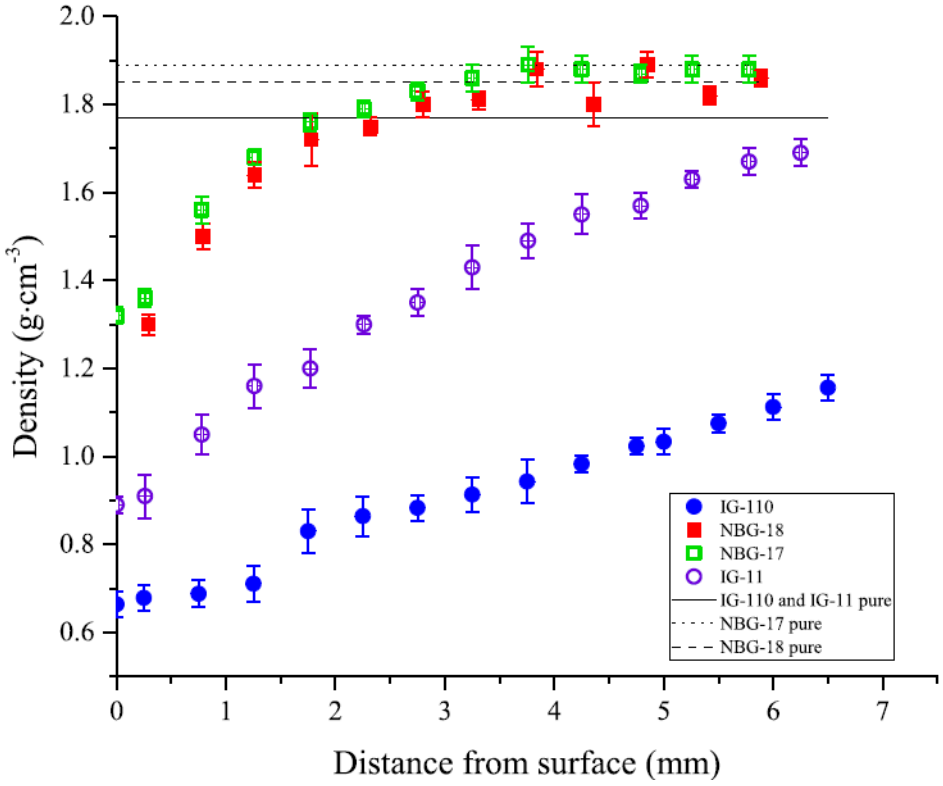

Fig. C.3 Density profiles in subsurface region of graphite grades IG-11, NBG-18, NBG-17, and IG-11 oxidized at 700 °C up to approximately 10 – 11 % WL. All measurements were performed using the lathing procedure. The core of oxidized IG-110 has lower density than the virgin material, showing that the penetration depth was comparable to (or larger than) half the diameter of unoxidized specimens (19.1 mm). (Reproduced from ref. [18] with permission.)

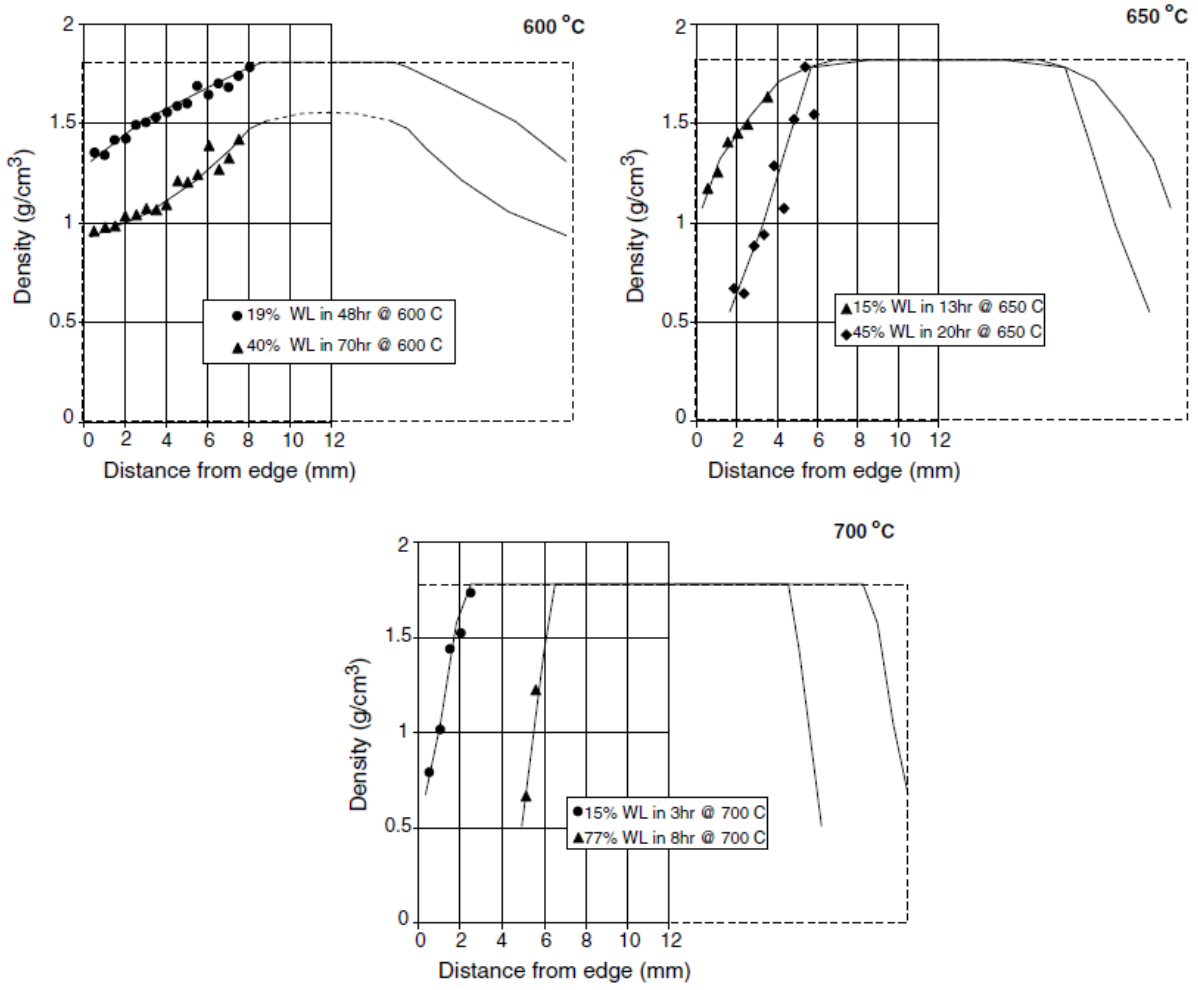

Fig. C.4 Density profiles in the subsurface region of graphite R4-650 oxidized at 600, 650, and 700 °C at two WL levels. The initial specimens were cylinders with Ø = h = 25.4 mm. Measurements were performed using the lathing procedure. Oxidant penetration depths after high WL levels oxidation at 600 °C and 650 °C are comparable to (or larger than) half the diameter of original specimens, resulting in lower densities at the oxidized specimens' core compared with the unoxidized specimens. (Data from ref. [16].)

REFERENCES

1 M. Srinivasan, Design and manufacture of graphite components for 21st century small modular reactors, Nucl. Eng. Des., 386 (2022) 111568. https://doi.org/10.1016/j.nucengdes.2021.111568.

2 T. Hicks, Modular HTGR safety basis and approach, INL/EXT-11-22708. Idaho National Laboratory, (2011). https://doi.org/10.2172/1027940.

3 ASME BPVC.III.5-2023, American Society of Mechanical Engineers, Boiler and Pressure Vessel Code, Section III, Division 5, Title HHA-3141 (2023).

4 J. Clark, R.E. Woodley, D.R. de Halas, Gas-graphite systems, in "Nuclear Graphite", Chapter 14, R.E. Nightingale (Editor), Academic Press, 1962.

5 HTGR, Preliminary safety information document for the standard MHTGR, DOE/HTGR-86-024-Vol. 1. Publ. Stone & Webster Engineering Corp. (1986).

6 F.A. Siladi, A.C. Millunzi, Safety aspects of the modular high-temperature gas-cooled reactor (MHTGR), GA-A-19823. General Atomics (1989). https://www.osti.gov/search/semantic:GA-A-19823.

7 N. Sakaba, T. Furusawa, T. Kawamoto, Y. Ishii, Y. Oota, Short design descriptions of other systems of the HTGR, Nucl. Eng. Des., 233 (2004) 147-154. https://doi.10.1016/j.nucengdes.2004.08.024.

8 C. Contescu, Validation of Wichner predictive model for chronic oxidation by moisture of nuclear graphite, ORNL/TM-2019/1306. Oak Ridge Nuclear Laboratory (2019). https://doi.org/10.2172/1606941.

9 M. B. Richards, Reaction of nuclear grade graphite with low concentrations of steam in the helium coolant of an MHTGR, Fuel, 15 (1990) 729-739. https://www.sciencedirect.com/science/article/abs/pii/036054429090112F.

10 M. Richards, HTR2016, International Topical Meeting on High Temperature Reactor Technology, Las Vegas, NV, November 6-10, 2016.

11 X. Yu, L. Brissonneau, Ch. Bourdeloie, S. Yu, The modeling of graphite oxidation behavior for HTGR fuel coolant channels under normal operating conditions, Nucl. Eng. Des., 238 (2008) 2230-2238. https://doi:10.1016/j.nucengdes.2008.02.022.

12 C. Wang, X. Sun, R. D. Christensen, Multiphysics simulation of moisture-graphite oxidation in MHTGR, Annals Nucl. Energy, 131 (2019) 483-495. https://doi.org/10.1016/j.anucene.2019.03.040.

13 S.S. Penner, M.B. Richards, Oxidation of nuclear-reactor-grade graphite, Energy, 13 (1988) 461-468. https://www.sciencedirect.com/science/article/abs/pii/0360544288900011,

14 R.P. Wichner, S. Ball, Potential damage of gas-cooled graphite reactors due to severe accidents, ORNL/TM-13661. Oak Ridge National Laboratory (1999). https://doi.org/10.2172/1910304.

15 H-K. Hinssen, K. Kühn, R. Moormann, B. Schlögl, M. Fechter, M. Mitchell, Oxidation experiments and theoretical examination on graphite materials. Nucl. Eng. Des., 238 (2008) 3018-3025. https://doi:10.1016/j.nucengdes.2008.02.013.

16 C.I. Contescu, S. Azad, D. Miller, M.J. Lance, F.S. Baker, T.D. Burchell, Practical aspects for characterizing air oxidation of graphite, J. Nucl. Mater., 381 (2008) 15-24. https://doi:10.1016/j.jnucmat.2008.07.020.

17 C.I. Contescu, J.P. Strizak, T.R. Guldan, T.D. Burchell, Effect of air oxidation on pore structure development and mechanical properties of nuclear graphite, ORNL/TM-2010/197. Oak Ridge National Laboratory (2010). https://doi.org/10.2172/1760103.

18 J.J. Lee, T.K. Ghosh, S.K. Loyalka, Comparison of NBG-18, NBG-17, IG-110 and IG-11 oxidation kinetics in air, J. Nucl. Mater., 500 (2018) 64-71. https://doi.org/10.1016/j.jnucmat.2017.11.053.

19 R.P. Wichner, T.D. Burchell, C.I. Contescu, Penetration depth and transient oxidation of graphite by oxygen and water vapor, J. Nucl. Mater., 393 (2009) 518-521. https://doi:10.1016/j.jnucmat.2009.06.032.

20 J. Kane, C. Karthik, R. Ubic, W.E. Windes, An oxygen transfer model for high purity graphite oxidation, Carbon 29 (2013) 49-64. http://dx.doi.org/10.1016/j.carbon.2013.02.053.

21 M.S. El-Genk, J.-M. P. Tournier, Comparison of oxidation model predictions with gasification data of IG-110, IG-430, and NBG-25 nuclear graphite, J. Nucl. Mater., 420 (2012) 141-158. http://doi.10.1016/j.jnucmat.2011.09.027.

22 M.S. El-Genk, J.-M. P. Tournier, C.I. Contescu, Chemical kinetics parameters and model validation for the gasification of PCEA nuclear graphite, J. Nucl. Mater., 444 (2014) 112-128. http://dx.doi.org/10.1016/j.jnucmat.2013.09.031.

23 M.S. El-Genk, J.-M. P. Tournier, Transient gasification in an NBG-18 coolant channel of a VHTR prismatic fuel element, Progress Nucl. Energy, 64 (2013) 16-30. http://dx.doi.org/10.1016/j.pnucene.2012.11.004.

24 C.H. Oh, C. Davis, L. Siefken, R. Moore, J.C. No, J. Kim, G.C. Park, J.C. Lee, W.R. Martin, Development of safety analysis codes and experimental validation for a very high temperature gas-cooled reactor, INL/EXT-06-01362. Idaho National Laboratory (2006). https://doi.org/10.2172/911270.

25 C.H. Oh, E.S. Kim, H.S. Kang, H.C. No, N.Z. Cho, Experimental validation of stratified flow phenomena, graphite oxidation, and mitigation strategies of air ingress accidents, INL/EXT-09-16465. Idaho National Laboratory (2009). https://doi.org/10.2172/974349.

26 Y. Zheng, M.M. Stempniewicz, Investigation of NACOK air ingress experiment using different system analysis codes, Nucl. Eng. Des., 251 (2012) 423-432. https://doi.10.1016/j.nucengdes.2011.09/050.

27 W. Windes, G. Strydom, R. Smith, J. Kane, Role of nuclear grade graphite in controlling oxidation in modular HTGRs, INL/EXT-14-31720. Idaho National Laboratory (2014).

28 M.M. Stempniewicz, E.A.R. de Geus, F. Roelofs, M. Skrzypek, J. Malesa, P. Vacha, J. Pokorny, N. Kohtz, C. Pohl, Analysis of air ingress scenario in GEMINI+ plant, Nucl. Eng. Des., 399 (2022) 112030. https://doi.org/10.1016/j.nucengdes.2022.112030.

29 W. Xu, Y. Zheng, L. Shi, P. Liu, Oxidation analyses of massive air ingress accident of HTR-PM, Sci. Technol. Nucl. Inst., 2016, 6419124; http://dx.doi.org/10.1155/2016/6419124.

30 C.H. Oh, E.S. Kim, H.C. No, N.Z. Cho, Final report on experimental validation of stratified flow phenomena, graphite oxidation and mitigation strategies of air ingress accidents, INL/EXT-10-20759. Idaho National Laboratory (2011). https://doi.org/10.2172/1023463.

31 M. Ishihara, T. Iyoku, S. Shiozawa, T. Miki, N. Takikawa, Experimental study on structural integrity of oxidized support post for HTTR, in Technical Committee Meeting on Response of Fuel, Fuel Elements and Gas Cooled Reactor Cores under Accidental Air or Water Ingress Conditions, IAEA TECDOC-784, pp. 25-31 (1993). https://www.osti.gov/etdeweb/biblio/48674.

32 C.H. Oh, E.S. Kim, H.C. No, N.Z. Cho, Experimental validation of stratified flow phenomena, graphite oxidation and mitigation strategies of air ingress accidents, INL/EXT-08-14840. Idaho National Laboratory (2008). https://doi.org/10.2172/944881.

33 S.J. Ball, D.J. Nypaver, GRSAC user's manual, ORNL.TM-13697. Oak Ridge National Laboratory (1999). https://doi.org/10.2172/5612.

34 K. Wagner, B. Beeny, D. Luxat, MELCOR accident progression and source term demonstration calculations for HTGR, SAND2022-2750. Sandia National Laboratories (2022). https://doi.org/10.2172/1854083.

35 S. Kim, H.C. No, B.J. Kim, C.H. Oh, Estimation of graphite density and mechanical strength variation of VHTR during air-ingress accident, Nucl. Eng. Des., 238 (2008) 837-847. https://doi:10.1016/j.nucengdes.2007.08.002.

36 H.C. No, H.S. Lim, J. Kim, C. Oh, L. Siefken, C. Davis, Multi-component diffusion analysis and assessment of GAMMA code and improved RELAP5 code, Nucl. Eng. Des., 237 (2007) 997-1008. https://doi:10.1016/j.nucengdes.2006.10.020.

37 S. Ball, M. Richards, S. Shepelev, Sensitivity studies of air ingress accidents in modular HTGRs, Nucl. Eng. Des., 238 (2008) 2935-2942. https://:doi.org/10.1016/j.nucengdes.2008.02.021.

38 C.I. Contescu, R. Paul, Oxidation behavior and property degradation of nuclear graphite, ORNL/TM-2022/1839. Oak Ridge National Laboratory (2022). https://doi.org/10.2172/1860566.

39 R.P. Wichner, T.D. Burchell, C.I. Contescu, Note on graphite oxidation by oxygen and moisture, ORNL/TM-2008/230. Oak Ridge National Laboratory (2008). https://doi.org/10.2172/947597.

40 ASTM D7542-21 Standard test method for air oxidation of carbon and graphite in the kinetic regime, ASTM International, West Conshohocken, PA 19428-2959, United States.

41 R.C. Roberts, "Molecular diffusion of gases" available at https://web.mit.edu/8.13/8.13c/references-fall/aip/aip-handbook-section2s.pdf.

42 R.B. Evans, G.M. Watson, E.A. Mason, Gaseous diffusion in porous media at uniform pressure, J. Chem. Phys., 35 (1961) 2076-2083. https://doi.org/10.1063/1.1732211.

43 G.F. Hewitt, M.J. C. Moore, E.W. Sharratt, The diffusion of oxygen in nitrogen in the pores of graphite: The effect of oxidation on diffusivity and permeability, Carbon 8 (1970) 271-282. https://doi-org.proxy1.library.jhu.edu/10.1016/0008-6223(70)90068-0

44 N. Shah, J.M. Ottino, Transport and reaction in evolving, disordered composites. I. Gasification of porous solids, Chem. Eng. Sci., 42 (1987) 63-72. https://doi-org.proxy1.library.jhu.edu/10.1016/0009-2509(87)80210-5.

45 J.J. Kane, A.C. Matthews, C.J. Orme, C.I. Contescu, W.D. Swank, W.E. Windes, Effective diffusion coefficients of select ultra-fine, super-fine and medium grain nuclear graphite, Carbon, 136 (2018) 369-379. https://doi.org/10.1016/j.carbon.2018.05.003.

46 Q. Huang, R.-C. Li, L. Cheng, H-F. Huang, X.-T. Zhou, Depth profile analysis of oxidized nuclear graphite microstructure using micro-focused synchrotron X-ray diffraction, J. Mater. Sci., 57 (2022) 6320-6334. https://doi.org/10.1007/s10853-022-07044-8.

47 C.I. Contescu, T.D. Burchell, Characterization of porosity development in oxidized graphite using automated-image analysis techniques, ORNL/TM-2009/192. Oak Ridge National Laboratory (2009). https://doi.org/10.2172/970899.

48 J. Kane, C. Karthik, D.P. Butt, W.E. Windes, R. Ubic , Microstructural characterization and pore structure analysis of nuclear graphite, J. Nucl. Mater., 415 (2011) 189–197. https://doi-org.proxy1.library.jhu.edu/10.1016/j.jnucmat.2011.05.053.

49 S.H. Chi, G.-C. Kim, Comparison of the oxidation rate and degree of graphitization of selected IG and NBG nuclear graphite grades, J. Nucl. Mater., 381 (2008) 9–14. https://doi-org.proxy1.library.jhu.edu/10.1016/j.jnucmat.2008.07.027.

50 C.I. Contescu, T. Guldan, P. Wang, T.D. Burchell, The effect of microstructure on air oxidation resistance of nuclear graphite, Carbon 50 (2012) 3354-3366. https://doi-org.proxy1.library.jhu.edu/10.1016/j.carbon.2012.01.040.

51 J.J. Q. Huang, T.K. Ghosh, S.K. Loyalka, Oxidation rate of nuclear-grade graphite IG-110 in the kinetic regime for VHTR air ingress accident scenarios, J. Nucl. Mater., 446 (2014) 38-48. https://doi-org.proxy1.library.jhu.edu/10.1016/j.jnucmat.2013.11.032.

52 J.J. Lee, T.K. Ghosh, S.K. Loyalka, Oxidation rate of nuclear-grade graphite NBG-18 in the kinetic regime for VHTR air ingress accident scenarios, J. Nucl. Mater., 438 (2013) 77-87. http://dx.doi.org/10.1016/j.jnucmat.2013.03.002. http://dx.doi.org/10.1016/j.jnucmat.2013.11.032.

53 C.I. Contescu, J.P. Strizak, T.R. Guldan, T.D. Burchell, Microstructure effect on air oxidation behavior of three nuclear graphite materials: NBG-18, PCEA, and IG-110, ORNL/TM-2011/324. Oak Ridge National Laboratory (2011).

54 J.J. Lee, T.K. Ghosh, S.K. Loyalka, Oxidation rate of nuclear-graphite IG-110 in the kinetic regime for VHTR air ingress accident scenarios, J. Nucl. Mater., 446 (2014) 38-48. http://dx.doi.org/10.1016/j.jnucmat.2013.11.032

55 X. Wei, S. Lei, Z. Yanhua, Transient analysis of nuclear graphite oxidation for high temperature gas cooled reactor, Nucl. Eng. Des., 306 (2016) 138-144. http://dx.doi.org/10.1016/j.jnucmat.2013.03.002.

56 B.H. Park, H.C. No, Strength degradation of oxidized graphite support column in VHTR, J. Nucl. Sci. Technol., 47 (2010) 998-1004. http://dx.doi.org/10.1016/j.jnucmat.2013.03.002.

57 J.B. Lim, E.S. Kim, C.H. Oh, R.R, Schultz, D.A. Petti, Computational assessment of the GT-MHR graphite core support structural integrity in an air-ingress accident condition, NUTHOS-7: The 7th International Topical Meeting on Nuclear reactor Thermal Hydraulics, Operation and Safety, Seoul, Korea, October 5-9, 2008; INL/CON-08-14466. https://www.osti.gov/search/semantic:INL/CON-08-14466.

58 R.M. Paul, C.I. Contescu, N.C. Gallego, R. Smith, J. Bass, J.J. Kane, A. Tzelepi, M. Metcalfe, On the thermal oxidation of nuclear graphite relevant to high-temperature gas cooled reactors, J. Nucl. Mater., 573 (2023) 154103. https://doi.org/10.2172/1860566.

59 M. Eto, F.B. Growcock, Effect of oxidizing environment on the strength of H451, PGX and IG-11 graphites, Carbon, 21 (1983) 135-147. https://doi-org/10.1016/0008-6223(83)90169-0.

60 S. Yoda, M. Eto, T. Oku, T. Sogabe, Effects of oxidation and tensile and compressive deformation behavior for nuclear-grades isotropic graphite, International Carbon Conference, Bordeaux (France), July 2-6, 1984.

61 S. Yoda, M. Eto, K. Tanaka, T. Oku, Effects of oxidation on compressive deformation behavior of nuclear-grade isotropic graphite, Carbon, 23 (1985) 33-38. https://doi-org./10.1016/0008-6223(85)90193-9.

62 S. Sato, K. Hirakawa, A. Kurumada, S. Kimura, E. Yasuda, Degradation of fracture mechanics properties of reactor graphite die to burn-off, Nucl. Eng. Des., 118 (1990) 227-241. https://doi-org./10.1016/0029-5493(90)90060-B.

63 A.C. Matthews, J.J. Kane, W.D. Swank, W.E. Windes, Nuclear graphite strength degradation under varying oxidizing conditions, Nucl. Eng. Des., 379 (2021) 111245. https://doi.org/10.1016/j.nucengdes.2021.111245

64 F.P. Knudsen, Dependence of mechanical strength of brittle polycrystalline specimens on porosity and grain size, J. Am. Ceram. Soc., 42 (1959) 376-387. https://doi.org/10.1111/J.1151-2916.1959.TB13596.X.

65 R.W. Rice, Comparison of physical property – porosity behavior with minimum solid area models, J. Mater. Sci., 31 (1996) 1509-1528. https://doi.org/10.1007/BF00357860.

66 E.L. Fuller, J.M. Okoh, Kinetics and mechanism of the reaction of air with nuclear grade graphites: IG-110, J. Nucl. Mater., 240 (1997) 241-250. https://doi-org.proxy1.library.jhu.edu/10.1016/S0022-3115(96)00462-X.

67 E.S. Kim, H.C. No, Experimental study on the oxidation of nuclear graphite and development of an oxidation model, J. Nucl. Mater., 349 (2006) 182-194. http://doi:10.1016/j.jnucmat.2005.10.015.

68 R. Yan, Y. Dong, Y. Zhou, X. Sun, Z. Li, Investigation of oxidation behaviors of nuclear graphite being developed and IG-110 based on gas analysis, J. Nucl. Sci. Technol., 54 (2017) 1168-1171. http://doi:10.1016/j.nucengdes.2003.11.004.

69 F.H. Ho, Graphite Design Handbook, DOE-HTGR-88111. General Atomics (1988). https://doi.org/10.2172/714896.

70 P. Hawtin, J.A. Gibson, The effect of diffusion and bulk gas flow on thermal oxidation of porous carbons. II – Diffusional effects in graphite, Carbon, 4 (1966) 489-500. https://doi.org/10.1016/0008-6223(66)90064-9.

71 C. Contescu, T. Burchell, Water vapor transport in nuclear graphite, ORNL/TM-2015/88. Oak Ridge National Laboratory (2015).

72 S.K. Bhatia, D.D. Perlmutter, A random pore model for fluid-solid reactions: I. Isothermal, kinetic control, AIChE J., 26 (1980) 379-386. https://doi.org/10.1002/aic.690260308.

73 R.M. Paul, J.D. Arregui-Mena, C.I. Contescu, N.C. Gallego, Effect of microstructure and temperature on nuclear graphite oxidation using the 3D random pore model, Carbon, 191 (2022) 132-145. https://doi.org/10.1016/j.carbon.2018.05.003